

## **Prestack V(z) f-k migration for P-P and P-S data**

Xinxiang Li and Gary F. Margrave

### **ABSTRACT**

V(z) f-k migration is a new f-k migration method based on non-stationary filter theory, which can handle the vertical velocity variation with at least the same accuracy as the phase-shift method. It retains the global wavefield mapping advantage of Stolt's method and properly accommodates the velocity variation. Instead of using a Fourier-domain complex-valued interpolation (as in Stolt's f-k method), V(z) f-k migration is formulated as a nonstationary filter, where the input for the filter is the f-k spectrum of the unmigrated seismic traces and the output is the spectrum of the migrated traces.

In this paper, the V(z) f-k migration is formulated for both P-P wave and P-S wave seismic data as a pre-stack migration method. In addition to some theory of the algorithm, the implementation detail is also presented.

The current implementation performs Fourier transform in CDP and offset dimensions. It only includes the migration up to 90 degree, and the evanescent energy is ignored. Some application results of this new method to synthetic data and field data are shown.

### **INTRODUCTION: CONVENTIONAL FOURIER DOMAIN MIGRATION METHODS**

#### **Derivation of Fourier domain migration formula from scalar wave equation**

The 2-D scalar wave equation is usually written as

$$\frac{\partial^2}{\partial t^2} \Psi(x, z, t) = v^2(x, z) \left[ \frac{\partial^2}{\partial x^2} + \frac{\partial^2}{\partial z^2} \right] \Psi(x, z, t) \quad (1)$$

Although this equation is based on some assumptions, it has been very successfully used for seismic data migration. Its derivation can be found in Claerbout (1985).  $\Psi$  represents a seismic wavefield as a function of  $x$  and  $z$ , the horizontal and vertical spatial dimensions, and time  $t$ .  $v(x, z)$  represents the wave propagation velocity at each spatial location. The velocity usually changes in both  $x$  and  $z$  directions, but it can still be assumed constant at any "local" area in  $(x, z)$  space. This local constant velocity concept is fundamental to Gazdag's phase-shift (Gazdag, 1978) and Stolt's f-k (Stolt, 1978) migration methods.

The wave field  $\Psi$  can be decomposed into harmonic plane waves in  $x$  and  $t$ , or mathematically expressed as an inverse Fourier transform (unless explicitly given, all the integration limits are from  $-\infty$  to  $\infty$  or over all possible values),

$$\Psi(x, z, t) = \iint \psi(k_x, z, \omega) \exp(-i\omega t + ik_x x) d\omega dk_x \quad (2)$$

Substituting (2) into (1), we have

$$\iint \left[ \frac{\omega^2}{v^2(x, z)} - k_x^2 - \frac{\partial^2}{\partial z^2} \right] \psi(k_x, z, \omega) \cdot \exp(-i\omega t + ik_x x) d\omega dk_x = 0 \quad (3)$$

If the velocity is independent to  $x$ , i.e.,  $v(x, z) = v(z)$ , then the term inside the brackets must be zero simply because only the zero function can have the zero function as its Fourier transform, i.e.,

$$\frac{\partial^2}{\partial z^2} \psi(k_x, z, \omega) = \left( k_x^2 - \frac{\omega^2}{v^2(z)} \right) \psi(k_x, z, \omega) \quad (4)$$

Within a local area where the velocity is constant, equation (4) can be solved analytically as

$$\psi(k_x, z, \omega) = A(k_x, \omega) \exp(ik_z z) + B(k_x, \omega) \exp(-ik_z z) \quad (5a)$$

where

$$k_z = \sqrt{\frac{\omega^2}{v^2(z)} - k_x^2} \quad (5b)$$

The functions  $A$  and  $B$  in equation (5a) are to be determined by initial or boundary conditions.

Equation (4) is equivalent to equation (1) only when the velocity is independent to  $x$ . Equation (5a) is a solution of equation (1) only when the velocity is constant. If the velocity changes, the accuracy of (5a) as a solution depends on how small the application area is and how rapidly the velocity changes.

The two terms the right side of equation (5a) represent upcoming and downgoing waves respectively. In seismic experiments, there is only one boundary condition, which is the seismic recording at the earth surface  $z=0$ . Using exploding reflector model (Claerbout, 1985), it is reasonable (for most cases) to consider that the downgoing wave path and the upcoming wave path are the same for zero offset. The zero offset traces can then be considered as the recorded seismic wavefield emerging from the subsurface reflectors with half the seismic velocity. This implies that picking the upcoming wave term in (5a) and using the boundary condition at zero depth will result in a reasonable solution of the wavefield at some non-zero depth. That is

$$\psi(k_x, z, \omega) = \psi(k_x, 0, \omega) \exp(-ik_z z) \quad (6)$$

Combine equations (2) and (6), the wavefield at depth  $z$  then can be expressed as an extrapolation from the wavefield at  $z=0$ ,

$$\Psi(x, z, t) = \iint \psi(k_x, 0, \omega) \exp(-ik_z z) \exp(-ik_x x + i\omega t) dk_x d\omega \quad (7)$$

The migration result (called imaging) is assumed to be the wavefield before the waves begin to propagate, i.e., the wavefield at time 0. Set  $t = 0$  in equation (7), then

$$\Psi(x, z, 0) = \iint \psi(k_x, z, \omega) \exp(-ik_x x) dk_x d\omega \quad (8)$$

Equation (6) and equation (8) are the starting point of the exploding-reflector-model based migration methods performed in Fourier domain. Gazdag's phase-shift method (Gazdag, 1978) and Stolt's f-k migration method (Stolt, 1978) are the original examples.

### Conventional Migration methods in Fourier domain

The phase-shift migration method can handle vertical velocity variation with plausible accuracy, because its wave extrapolation (downward continuation) is done within relatively thin layers, which can reasonably be considered as local areas where wave velocities are constant. This is to say that the assumptions required by equation (6) and equation (8) are reasonable in each of those layers.

In phase-shift migration, the process expressed by equation (6) is called phase-shift or wavefield downward extrapolation, while equation (8) is called the imaging condition. First, the Fourier transform is computed for the wavefield recorded at zero depth, then by equation (6) the spectrum at depth  $z = \Delta z$  is computed, which will be used to compute the spectrum at the new depth  $z = 2 \cdot \Delta z$  and so on. At each depth step, equation (8) is used to give the migration image at that depth level. More detail can be found in Gazdag (1978), Claerbout (1985), and Yilmaz (1987).

Stolt's f-k migration method (1978) is based on the assumption that the entire  $(x, z)$  plane is one area with constant velocity. In this case, the extrapolation process, equation (6) can be applied for any initial depth  $z_0$  and target depth  $z$ , and it is unnecessary to compute the wavefield at intermediate depth levels, because the phase shift term (equation (5a)) is now depth independent.

On the right side of equation (8), the integral over  $k_x$  is a Fourier transform, but the integral over  $\omega$  is not. The key innovation of Stolt's f-k method is to express  $\omega$  in terms of  $k_z$  and write the equation as a 2-D inverse Fourier transform. Note that  $\omega = v\sqrt{k_x^2 + k_z^2}$  (this is a mapping in 2-D Fourier domain), and  $d\omega = v \frac{k_z}{\sqrt{k_x^2 + k_z^2}} dk_z$

(this implies a scaling factor), equation (8) can be re-written as

$$\Psi(x, z, 0) = \iint \frac{vk_z}{\sqrt{k_x^2 + k_z^2}} \psi\left(k_x, 0, v\sqrt{k_x^2 + k_z^2}\right) \exp(ik_z z - ik_x x) dk_x dk_z \quad (9)$$

For clarity and later comparison, Stolt's method can be expressed as a 4-step algorithm:

**Step 1:** Fourier transform the surface data, i.e.,  $\Psi(x,0,\omega) \Rightarrow \psi(k_x,0,\omega)$ .

**Step 2:** Map data  $\psi(k_x,0,\omega)$  to  $\bar{\psi}(k_x,k_z) = \psi\left(k_x,0,v\sqrt{k_x^2+k_z^2}\right)$ .

**Step 3:** Scale  $\bar{\psi}(k_x,k_z)$  with  $v\frac{k_z}{\sqrt{k_x^2+k_z^2}}$  to obtain  $\bar{\bar{\psi}}(k_x,k_z)$ .

**Step 4:** Inverse 2-D Fourier transform, i.e.,  $\bar{\bar{\psi}}(k_x,k_z) \Rightarrow \Psi(x,z,0)$ .

The constant velocity assumption for Stolt's f-k method is not valid for almost all the seismic experiments, although Stolt's stretch (1978) may be suitable for the cases when the velocity changes smoothly with depth. With his non-stationary filter theory, Margrave (1998b) introduced a new f-k method, which handles the vertically variant velocity with at least the same accuracy as phase-shift method. The following section will give a short derivation of this method. Its extension to pre-stack migration for both PP wave data and PS wave data is discussed in more detail.

## V(z) F-K MIGRATION: POST-STACK AND PRE-STACK

### Extension of f-k method to vertical velocity variation

The key advantage of Stolt's f-k method is that the imaging process can be done in one step for the entire space by using Fourier transforms, and this makes the method the fastest migration algorithm known. However, equation (9) leaves no space to accommodate the depth (or time) variant properties.

Margrave (1998b) shows how equation (9) is related to a non-stationary filter, which can conveniently handle the vertical velocity variation. The frequency domain scaled mapping can be interpreted as a non-stationary transform from the frequency of input traces to the frequency (or depth wavenumber) of migrated output traces.

To obtain the wavefield at any depth  $z$ , equation (6) can not be directly used because the materials between surface and depth  $z$  may have different velocities. Gazdag's phase-shift is based on the assumption that, in each infinitesimally thin layer with thickness  $dz$ , the wave propagation velocity does not change. Using this assumption, equation (6) can be applied recursively to obtain

$$\psi(k_x,z,\omega) = \psi(k_x,0,\omega) \exp \left[ \left( -i \sum_{i=1}^n \sqrt{\frac{\omega^2}{v^2((i-1) \cdot dz)} - k_x^2} dz \right) + -i \cdot \sqrt{\frac{\omega^2}{v^2(n \cdot dz)} - k_x^2} \cdot \theta \cdot dz \right].$$

Where  $n$  is an integer such that  $z = n \cdot dz + \theta \cdot dz$  with  $\theta$  always smaller than 1.0. Taking the limit as  $dz$  approaches 0, the following equation results

$$\psi(k_x, z, \omega) = \psi(k_x, 0, \omega) \exp\left(-i \int_0^z \sqrt{\frac{\omega^2}{v^2(z')} - k_x^2} dz'\right) = \psi(k_x, 0, \omega) m(k_x, z, \omega) \quad (10)$$

This is equivalent to a first order WKBJ solution (Aki and Richards, 1980) of equation (4). It includes the effects of Snell's law at every velocity interface but neglects transmission losses. Substitute (10) into equation (8) and ignore the Fourier transform over  $k_x$  for now,

$$\psi(k_x, z, 0) = \int \psi(k_x, 0, \omega) m(k_x, z, \omega) d\omega \quad (11)$$

For each  $k_x$ , equation (11) is a non-stationary combination filter expressed in the mixed domain (Margrave, 1998a). The new method (called V(z) f-k migration) can be implemented based on this equation. However, it is good to see some results from the algorithms based on the Fourier domain non-stationary combination filter. Implementation of the mixed domain algorithm will be done later.

Fourier transform of equation (11) from  $z$  to  $k_z$  gives the following,

$$\theta(k_x, k_z) = \int \psi(k_x, 0, \omega) M(\omega, k_z, k_x) d\omega \quad (12a)$$

Where

$$M(\omega, k_z, k_x) = \int m(k_x, z, \omega) \exp(-ik_z z) dz = \int \exp\left(-i \int_0^z \sqrt{\frac{\omega^2}{v^2(z')} - k_x^2} dz'\right) \exp(-ik_z z) dz \quad (12b)$$

Equation (12a) is an expression of a non-stationary combination filter in the Fourier domain.  $m(k_x, z, \omega)$  in equation (11) and  $M(\omega, k_z, k_x)$  in equation (12a) can both be called migration filters.  $m$  is called the mixed domain filter while  $M$  is called the Fourier domain filter. Equations (12a) and (12b) suggest a new algorithm for migration in f-k domain, and it can be explicitly implemented in four steps:

**Step 1:** Fourier transform the surface data, i.e.,  $\Psi(x, 0, \omega) \Rightarrow \psi(k_x, 0, \omega)$ .

**Step 2:** Compute the migration filter  $M(\omega, k_z, k_x)$  for each  $k_x$ .

**Step 3:** Compute the 2-D transformed image, i.e.,  $\theta(k_x, k_z)$ ;

**Step 4,** Inverse 2-D Fourier transform, i.e.,  $\theta(k_x, k_z) \Rightarrow \Psi(x, z, 0)$ .

Comparing to the 4-step algorithm for Stolt's method, the differences reside in **Step 2** and **Step 3**, while the Fourier transforms in **Step 1** and **Step 4** are the same. The purpose of the **Step 2** and **Step 3** in both algorithms are to properly transform the input data f-k spectrum to the f-k spectrum of migration data. Besides the capability of properly handling the velocity variation, using non-stationary filters in this new algorithm has another advantage. It avoids Fourier domain mapping required in Stolt's method, which involves complex-valued interpolation (Claerbout, 1985) and

might result in many artifacts if is not handled properly. However, the computation and the application of migration filters in **Step 2** and **Step 3** consume more computation time than the mapping and scaling in Stolt's method.

To understand what the migration filters do, Margrave (1998b) shows how migration filter theoretically coincides with the mapping and scaling in Stolt's method when the velocity is constant. An intuitive point of view is that, the migration impulse responses (called "smiles") change their shapes when the impulse changes its time location, even for constant velocity cases.

### Extension to pre-stack with mode conversion

Wavefield extrapolation in the common mid-point,  $x$ , and source-receiver half-offset,  $h$ , domain can be expressed as (Claerbout, 1985)

$$\Psi(x, h, z, t) = \iiint \psi(k_x, k_h, z, \omega) \exp(i(\omega t - k_x x - k_h h)) dk_x dk_h d\omega, \quad (13a)$$

where

$$\begin{aligned} \psi(k_x, k_h, z, \omega) = \\ \psi(k_x, k_h, 0, \omega) \exp \left( -i \cdot z \left\{ \sqrt{\frac{\omega^2}{v_S^2} - \left(\frac{k_x - k_h}{2}\right)^2} + \sqrt{\frac{\omega^2}{v_R^2} - \left(\frac{k_x + k_h}{2}\right)^2} \right\} \right) \end{aligned} \quad (13b)$$

for constant velocity cases. The two square root terms correspond to the wavefield downward continuations for both downgoing waves from the source and upcoming waves to the receiver respectively. Use the first order WKBJ approximation as for the deviation of equation (10), (13b) for vertical velocity variation case can be approximated as

$$\begin{aligned} \psi(k_x, k_h, z, \omega) = \\ \psi(k_x, k_h, 0, \omega) \exp \left( -i \int_0^z \left\{ \sqrt{\frac{\omega^2}{v_S^2(z')} - \left(\frac{k_x - k_h}{2}\right)^2} + \sqrt{\frac{\omega^2}{v_R^2(z')} - \left(\frac{k_x + k_h}{2}\right)^2} \right\} dz' \right). \end{aligned} \quad (13c)$$

where  $v_S$  and  $v_R$  are velocities for downgoing ( $S$  stands for source) and upcoming waves ( $R$  stands for receiver). The migration result (imaging), which is the wavefield at time  $t=0$  and offset  $h=0$ , can then be expressed as

$$\Psi(x, 0, z, 0) = \iiint \psi(k_x, k_h, z, \omega) \exp(-ik_x x) dk_x dk_h d\omega. \quad (14)$$

Ignoring the integral over  $k_x$  and  $k_h$  for now, and Fourier transforming in  $z$  direction, it gives

$$\theta(k_x, k_z) = \iint \psi(k_x, k_h, 0, \omega) M(\omega, k_z, k_x, k_h) dk_h d\omega \quad (15a)$$

where

$$M(\omega, k_z, k_x, k_h) = \int \exp \left[ -i \left( \int_0^z \left\{ \sqrt{\frac{\omega^2}{v_S^2(z')} - \left( \frac{k_x - k_h}{2} \right)^2} + \sqrt{\frac{\omega^2}{v_R^2(z')} - \left( \frac{k_x + k_h}{2} \right)^2} \right\} dz' - k_z z \right) \right] dz. \quad (15b)$$

Similar to post-stack case (equation (12a)), a new pre-stack f-k migration algorithm based on equation (15a) can be explicitly expressed as following four steps.

**Step 1**, Fourier transform the recorded surface seismic data in three dimensions, i.e.,  $\Psi(x, h, 0, \omega) \Rightarrow \psi(k_x, k_h, 0, \omega)$ ;

**Step 2**, Compute the migration filter  $M(\omega, k_z, k_x, k_h)$ , as defined in (15b) for given  $k_x$  and  $k_h$ ;

**Step 3**, Use equation (15a) to compute the 2-D Fourier transform of the migrated image, i.e.,  $\theta(k_x, k_z)$ ;

**Step 4**, Inverse 2-D Fourier transform to obtain the final migration, i.e.,  $\theta(k_x, k_z) \Rightarrow \Psi(x, z, 0)$ .

## CONSIDERATIONS FOR ALGORITHM IMPLEMENTATION

The implementations for the algorithms of post-stack and pre-stack migration by the direct V(z) f-k method are very similar. The discussions in this section mainly deal with the pre-stack case, the post-stack case implementation will be mentioned when there is significant difference.

Even though we tried to reduce the computation cost in many aspects, the present algorithm is still time consuming. Other ways to simplify the computation are in the context of further research.

### Computation of the migration filter in Fourier domain

The computation and application of the migration filters is the main difference of present method from the conventional migration methods in Fourier domain. Also, it is the most time-consuming part of the algorithm.

In the four-step algorithm described above, the input to Step 2 (the computation of migration filters) consists of the “traces” which are Fourier transformed in 3 dimensions. For the post-stack case, such a trace is a vector with its elements representing the temporal frequency spectrum for a fixed wavenumber  $k_x$ , and different traces correspond to different wavenumbers. For the pre-stack case, such a trace represents the temporal frequency spectrum for fixed pair of wavenumbers denoted by  $(k_x, k_h)$ . Different traces correspond to different wavenumber pairs. Like

many other normal seismic data processing methods, the computation and application of migration filters is designed to operate in a trace-by-trace manner.

### *Same migration filter for a group of input traces*

Major computation cost savings arise because the computation of the migration filter does not have to repeat for each input trace. The following discussion shows that, some different pairs of  $k_x$  and  $k_h$  have identical migration filters.

From equation (15b), the definition of the migration filter for the prestack case,  $M(\omega, k_z, k_x, k_h)$ , as a function of  $k_x$  and  $k_h$ , has some symmetry, that is

$$M(\omega, k_z, k_x, k_h) = M(\omega, k_z, -k_x, -k_h)$$

This means that, for the case of pre-stack algorithm with mode-conversion, any two traces representing opposite-sign horizontal wavenumber  $k_x$  and opposite-sign offset wavenumber  $k_h$  have the same migration filter. For every two traces, only one migration filter needs to be computed, so that the total computation is reduced by half.

If the down-going and up-coming velocities are the same, i.e., no wave mode conversion is present, more symmetry in equation (15b) occurs. This is

$$M(\omega, k_z, k_x, k_h) = M(\omega, k_z, |k_x|, |k_h|)$$

Thus, four different input traces with four different pairs of  $(k_x, k_h)$  with the same value pair  $(|k_x|, |k_h|)$  have the same migration filter. This reduces the total computation cost by almost 75%.

### *Phase-shift term pre-computation using sampled ray parameters*

It is instructive to re-write equation (15b) into

$$M(\omega, k_z, k_x, k_h) = \int \exp[-i \cdot \zeta(z, \omega, k_x, k_h)] \exp(+ik_z z) dz \quad (16)$$

where

$$\zeta(z, \omega, k_x, k_h) = \int_0^z \sqrt{\frac{\omega^2}{v_S^2(z')} - \left(\frac{k_x - k_h}{2}\right)^2} + \sqrt{\frac{\omega^2}{v_R^2(z')} - \left(\frac{k_x + k_h}{2}\right)^2} dz' \quad (17)$$

**Step 2** is then subdivided as follows:

**Step 2-1:** For every input trace with fixed  $k_x$  and  $k_h$ , compute the phase-shift term  $\zeta(z, \omega, k_x, k_h)$  as a function of both depth  $z$  and temporal frequency  $\omega$ . Then multiply  $\zeta(z, \omega, k_x, k_h)$  with  $-i$  and calculate the exponential.

**Step 2-2:** Fourier transform in  $z$  for each  $\omega$ . This may take the majority of the computation time.

Equation (17) can be further re-formatted as

$$\begin{aligned} \zeta(z, \omega, k_x, k_h) &= \omega \cdot \int_0^z \left[ \sqrt{\frac{1}{v_S^2(z')} - \left(\frac{k_x - k_h}{2\omega}\right)^2} + \sqrt{\frac{1}{v_R^2(z')} - \left(\frac{k_x + k_h}{2\omega}\right)^2} \right] dz' \\ &= \omega \cdot \left[ \int_0^z \sqrt{\frac{1}{v_S^2(z')} - p_1^2(\omega, k_x, k_h)} dz' + \int_0^z \sqrt{\frac{1}{v_R^2(z')} - p_2^2(\omega, k_x, k_h)} dz' \right] \\ &= \omega \cdot [\zeta_1(z, \omega, k_x, k_h) + \zeta_2(z, \omega, k_x, k_h)]. \end{aligned} \quad (17b)$$

Although the ray parameters  $p_1$  and  $p_2$  depend on variables  $\omega$ ,  $k_x$  and  $k_h$ , they can be tabulated as

$$p_1 = \{0, \Delta p_1, 2\Delta p_1, \dots, (N_p - 1)\Delta p_1\} \quad \text{and} \quad p_2 = \{0, \Delta p_2, 2\Delta p_2, \dots, (N_p - 1)\Delta p_2\}$$

The number of ray parameters  $N_p$  or the sample intervals  $\Delta p_1$  and  $\Delta p_2$  can be determined by practical application testing. The limiting parameters are determined by observed velocities.

$$p_1 \in \left[0, \frac{1}{\min(v_S)}\right] \quad \text{and} \quad p_2 \in \left[0, \frac{1}{\min(v_R)}\right].$$

Two tables for  $\zeta_1$  and  $\zeta_2$  can then be formed using equation (17) at discrete depth and ray-parameter locations and they can be used for all the input traces. For each pair of  $(k_x, k_h)$ , either the nearest sampled ray parameter or linear interpolation between the nearest two ray parameters in the tables can be used. This saves many square-root operations.

Although the total number of possible different ray parameters is close to the product of three large numbers, (i.e., the numbers of possible  $\omega$ ,  $k_x$  and  $k_h$  respectively), practically, it suffices to tabulate a number similar to the number of the samples of an input trace. The accuracy is usually very good. For example, we have used 500 ray parameters for 500-sample input traces, while the number of offset and CDP wavenumbers are both around 100. The relative differences between the accurate phase-shift terms calculated by directly using equation (17) and the phase-shift terms by linear interpolation of phase-shift tables are less than 0.1 percent.

Notice that for both non-mode-conversion and post stack case, only one phase shift table is needed because there is only one velocity function.

In addition, the computation of phase-shift terms is further constrained by the evanescent energy limit, maximum frequency and maximum dip to migrate. These limitations are discussed in the next section.

Zero elements in migration filter matrices

In equation (17b), for each given  $\omega$ ,  $k_x$  and  $k_h$ ,  $\zeta(z, \omega, k_x, k_h)$  is a function of  $z$  limited by the following two numbers,

$$\zeta_{min} = \omega \cdot \left[ \sqrt{\frac{1}{\max(v_S^2)} - p_1^2} + \sqrt{\frac{1}{\max(v_R^2)} - p_2^2} \right],$$

and

$$\zeta_{max} = \omega \cdot \left[ \sqrt{\frac{1}{\min(v_S^2)} - p_1^2} + \sqrt{\frac{1}{\min(v_R^2)} - p_2^2} \right].$$

This means the migration filter  $M$  in equation (16), as a function of depth-wavenumber  $k_z$ , has non-zero values only within the interval  $k_z \in [\zeta_{min}, \zeta_{max}]$ . The difference between  $\zeta_{min}$  and  $\zeta_{max}$  only depends on the difference between the maximum and the minimum velocities. If the velocity is constant, we only need to compute phase-shift terms at one wavenumber  $k_z = \zeta_{min} = \zeta_{max}$  for given  $\omega$ ,  $k_x$  and  $k_h$ . (Actually, the algorithm can reduce to the Stolt's f-k migration in this case.)

Migration filters are 2-variable functions of depth wavenumber  $k_z$  and temporal frequency  $\omega$  for each pair of  $k_x$  and  $k_h$ . Figure 1 shows two examples of migration filters for constant velocity cases. (a) shows a migration filter for a same upcoming and downgoing velocity, and (b) shows a migration filter mode-conversion case. Figure 2 shows two migration filters for velocities with linearly vertical variation. Again, (a) is for the non-mode-conversion case, and (b) is for the converted wave case. The white lines in both Figure 1 and Figure 2 are the curves corresponding to the limits  $[\zeta_{min}, \zeta_{max}]$ . When the velocities are constant, these two values become the same.

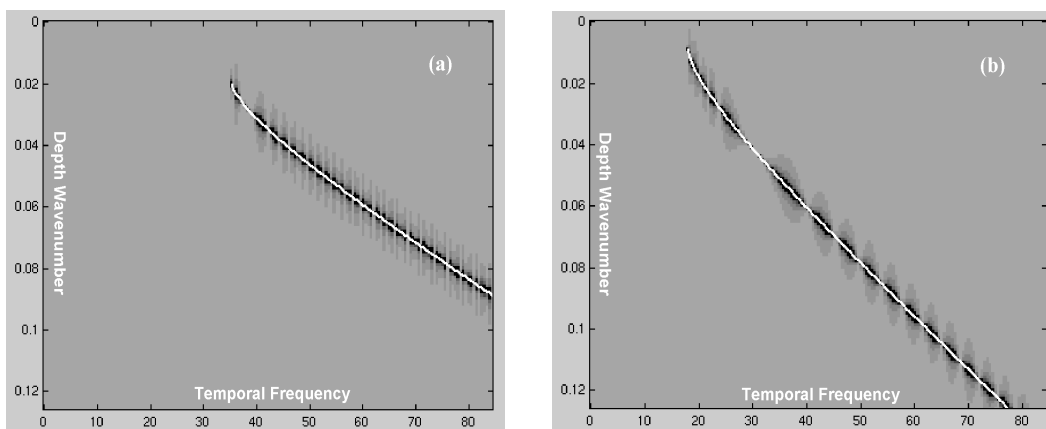


Figure 1: Two migration filters for constant velocity cases. In (a), the downgoing and upcoming wave velocities are all equal to 1800 m/s. In (b) the downgoing wave velocity is 1800 m/s and the upcoming wave velocity is 900 m/s. For both cases, the migration filters are computed for the same  $k_x$  and  $k_h$  values

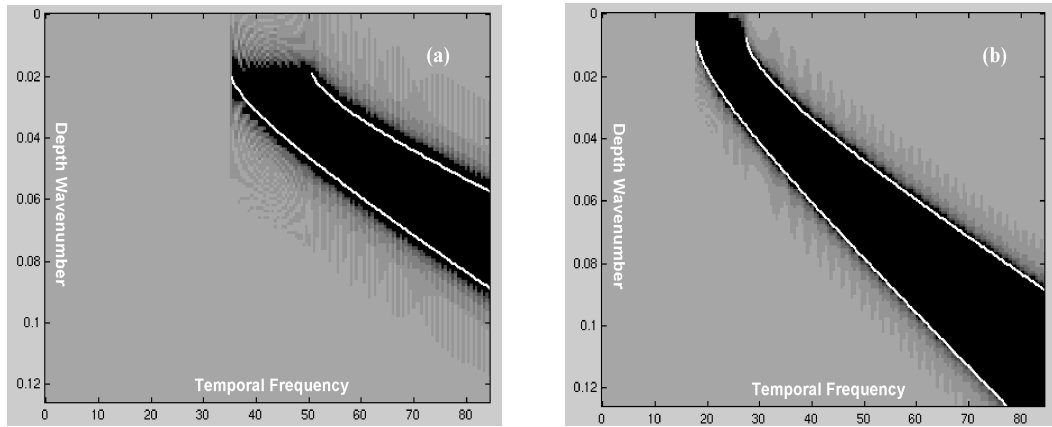


Figure 2: Two migration filters for linearly varying velocity cases. The filter in (a) is calculated for the non-mode-conversion case, where the velocity is  $1800+0.8z$ . The filter (b) is calculated for different upcoming and downgoing velocities, they are  $1800+0.8z$  and  $900+0.5z$  respectively. Again, the two migration filters are computed for the same  $k_x$  and  $k_h$ .

It can be seen that, for all the four migration filters, the non-zero values can not be totally limited by the boundary curves. This is because the mapping from  $\omega$  to  $k_z$  is not a simple one to-one relation. To determine an output at certain  $k_z$ , a range of  $\omega$  is needed. This is related to both the Fourier domain interpolation and the non-stationary filter in Fourier domain. For the constant velocity cases, if the Fourier domain interpolation is used, it turns out to be Stolt's method. The advantage of  $V(z)$  f-k method is that, the Fourier domain interpolation is replaced by full range Fourier transform, and it obtains the highest possible accuracy for any interpolation algorithm.

In Stolt's f-k method, the Fourier transformed traces are mapped from input temporal frequency  $\omega$  to output depth wavenumber  $k_z$  (or out migrated temporal frequency). The new algorithm achieves a similar mapping since a migration filter is a linear transform from input  $\omega$  space to output  $k_z$  space.

Figure 1 and Figure 2 show that, for single input trace with fixed  $(k_x, k_h)$ , the migration filter performs a different mapping for different velocities. When a trace is migrated with higher velocity the output frequency range tends to be lower and vice versa. This implies that if P-P and P-S data have the same frequency bandwidth, the migration of the P-S data tends to have broader  $k_z$  bandwidth than that of the migrated P-P data. On the other hand, for given migration velocity functions, migration filters for different ray parameters (which correspond to different pairs of  $(k_x, k_h)$ ) have different non-zero zones. Larger ray parameters tend to map the data to lower frequency. An extreme case occurs when the ray parameter is too large and out of the range determined by the reciprocal of the minimum velocity. Then, the migration filter is evanescent and can be simply set to zero. Thus a trace  $(k_x, k_h)$  corresponding to too large ray parameter will not be migrated.

Efficient computation of the upper and lower limits of  $k_z$  suggests that many multiplication operations for **Step 3** (refer to page 9) in the algorithm are unnecessary. Unfortunately, the computation cost of **Step 3** is much less compared

with **Step 2**, the cost-saving by limiting  $k_z$  practically does not make much difference. Also, it adds some computations for the limits themselves. However, if we only computed the migration filter between the  $k_z$  limits by some approximation, then we would save much more time. Currently, the computation of migration filter is done by Fourier transforms of the filter in mixed domain (refer to equations (11) and (12)).

## Migration limitations

### *Evanescent energy*

Evanescent waves are those wave-equation solutions that decay exponentially in the spatial domain instead of oscillating in a sinusoidal manner. The exponentially decaying waves quickly become neglectable and are often simply eliminated, although it is simple to include the evanescent energy in many migration methods. The current implementation does not include this energy.

For a laterally uniform medium with velocity changes only in depth, the evanescent solutions are those which make  $k_z$  imaginary. For the post-stack case, equation (5b) gives a condition for evanescent energy as

$$|\omega| < |k_x| \cdot v(z) \quad (18)$$

This is a localized condition since it gives a different limitation on the range of  $k_x$  and  $\omega$  depending on the local velocity. A Fourier plane wave propagates with a sinusoidal waveform at low velocity regions, and will turn into a decaying exponential when the propagation velocity goes high enough to make inequality (18) valid.

For pre-stack case, equation (13b) shows  $k_z$  to be

$$\begin{aligned} k_z &= \sqrt{\frac{\omega^2}{v_S^2(z)} - \left(\frac{k_x - k_h}{2}\right)^2} + \sqrt{\frac{\omega^2}{v_R^2(z)} - \left(\frac{k_x + k_h}{2}\right)^2} \\ &= \sqrt{\frac{\omega^2}{v_S^2(z)} - k_s^2} + \sqrt{\frac{\omega^2}{v_R^2(z)} - k_r^2}, \end{aligned} \quad (19)$$

so the evanescent energy conditions for both downgoing and upcoming waves are similar to the post-stack case, equation (18). However, from equation (19), when a downgoing plane wave identified by  $(\omega, k_d)$ , for example, becomes evanescent at some depth  $z$ , the upcoming wave with this same frequency, i.e., the one identified by  $(\omega, k_r)$ , may still be sinusoidal at this depth.

During the downward continuation, if the evanescent energy from the downgoing (for example) part of the wavefield were ignored, then there would be no energy transmitting beyond some depth level where all the waves become evanescent. By the imaging condition of the migration process, downward continuation of the upcoming wave should also stop at this depth. Thus, it seems reasonable to treat the entire

operator ( $\exp(ik_z \Delta z)$ ) as evanescent when either square root in equation (19) becomes imaginary. This leads to the evanescent condition we are using for pre-stack case:

$$|\omega| < \frac{1}{2} \max\{v_S(z) \cdot |k_x - k_h|, v_R(z) \cdot |k_x + k_h|\} \quad (20a)$$

When the two velocities are the same, (20a) is simply

$$|\omega| < \frac{1}{2} v(z) \cdot (|k_x| + |k_h|) \quad (20b)$$

Equations (20a) and (20b) are the limitations used in the current algorithm.

### *Migration dip limitation*

A limitation on migration dip is actually a limitation on the range of ray parameters. For a given value of horizontal spatial wavenumber  $k_x$  for post-stack case or  $k_s$  and  $k_r$  for pre-stack case, this limitation becomes a limitation on the temporal frequency  $\omega$ . The limitations can be written as

$$|\omega| > \frac{1}{2} \cdot \frac{v(z) \cdot |k_x|}{\sin(\theta_{max})} \quad (21)$$

for the post-stack case, where the velocity is half of the wave velocity, and

$$|\omega| > \frac{1}{2} \frac{\max\{v_S(z) \cdot |k_x - k_h|, v_R(z) \cdot |k_x + k_h|\}}{\sin(\theta_{max})} \quad (22)$$

for the pre-stack case. Where  $\theta_{max}$  is the maximum dip to migrate.

Comparing (21) and (22) with (18) and (20) shows that the limitations of evanescent energy are special cases of the dip limitations. In this way, the evanescent energy can be understood as that with ray angle greater than 90 degrees.

### *Frequency limitation*

Usually for computational efficiency reasons, it is desirable to limit the frequency range for the migration process. That is, if the vast majority of the seismic energy resides inside 80Hz, then it is unnecessary to migrate the frequencies beyond 80Hz. Frequency limitation is always uniform for all the wavenumbers and usually applied only at the high-frequency end.

As discussed above, the limitations related to evanescent energy and migration dip can be also considered as limitations on temporal frequency. These limits on frequency change with spatial wavenumbers and other parameters, and they always are limitations at the low-frequency end.

### Special consideration for mode-conversion

In  $V(z)$  f-k algorithm, the pre-stack migration for mode-converted cases introduces some specific difficulties.

#### *Wavefield extrapolation formulation*

The imaging condition for downward wavefield extrapolation results in some restrictions on our formulation. The imaging condition for the prestack case is equivalent to putting source and receiver physically together (set both offset and time to zero) at each extrapolation depth level. This implies that before we perform the imaging process, both sources and receivers must be at the same physical depth level. For non-mode-conversion case, because the propagation velocities for both downgoing and upcoming waves are the same, the survey-sinking process (Claerbout, 1985) can be done either in depth or in vertical traveltime. But for the mode-converted case, to express the downward extrapolation in time steps, then the physical depths for P-waves and S-waves “sunk” by the extrapolation processes will be different, and then no imaging condition can be applied in this situation. This means, the algorithm for mode-conversion case should be directly formulated in depth domain.

When downgoing and upcoming velocities are different, it is not difficult to formulate the equations into whatever time domain desired (PP time, PS time or even SS time). However, at every downward extrapolation step, waves with lower velocities take longer time than the waves with higher velocity. It is equivalent to the depth to time conversion after the migration is done.

#### *Offset orientation*

For the non-mode-conversion case, the directions of the source-receiver offsets do not make any difference in the migration process when the velocity changes only in depth. However, for the mode-converted case, there are differences.

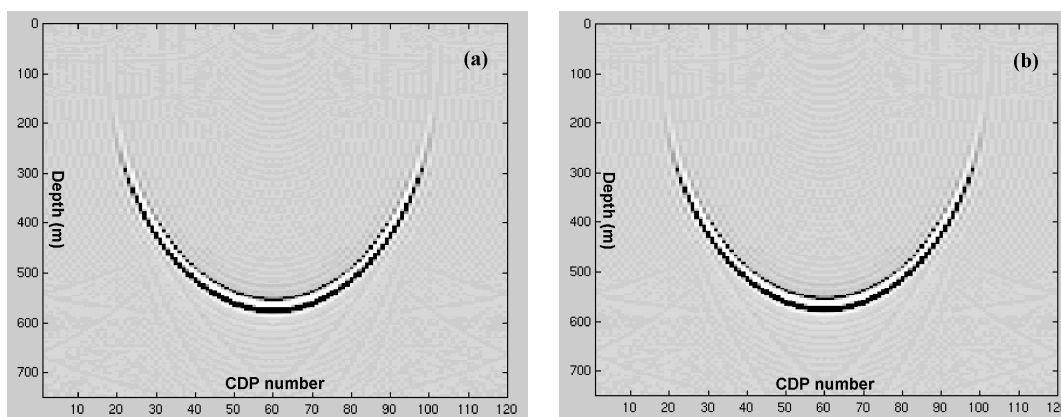


Figure 3: Impulse responses of  $V(z)$  f-k migration method for non-conversion data. The input trace for the response in (a) has one impulse at time 582 ms with offset equal to 275 meters. The input trace for the response in (b) has one impulse also at time 582 ms but with offset equal to -275 meters. The velocity functions used to migrate the two traces are the same,  $1800+0.8*z$  m/s. The difference of these two responses is shown in Figure 5(a).

Figure 3 and Figure 4 show the results from the migration of a synthetic trace with only one impulse. Positive and negative offsets are assigned to this trace. As expected, there is no identifiable differences between the results from non-mode-conversion case, they both give symmetric ellipses (Figure 3). While the migration response results for converted waves, the “ellipses” are stretched in opposite different directions (always stretched to the direction of lower velocity) (Figure 4).

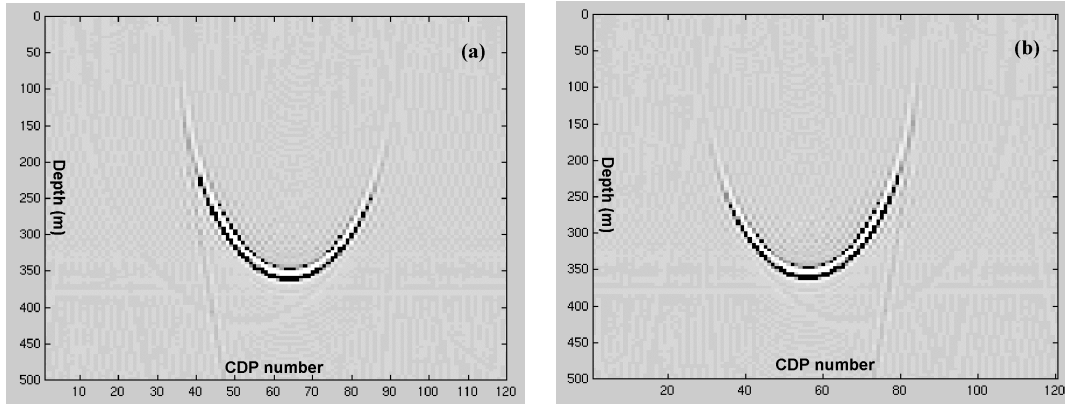


Figure 4: Impulse responses of  $V(z)$  f-k migration method for converted wave data. The input trace for the response in (a) has one impulse at time 582 ms with offset equal to 275 meters. The input trace for the response in (b) has one impulse also at time 582 ms but with offset equal to -275 meters. The velocity functions used to migrate the two traces are the same. For downgoing waves, the velocity is  $1800+0.8*z$  m/s and for upcoming waves, the velocity is  $900+0.5*z$  m/s. The superposition of these two responses are shown in Figure 5(b) for their position difference.

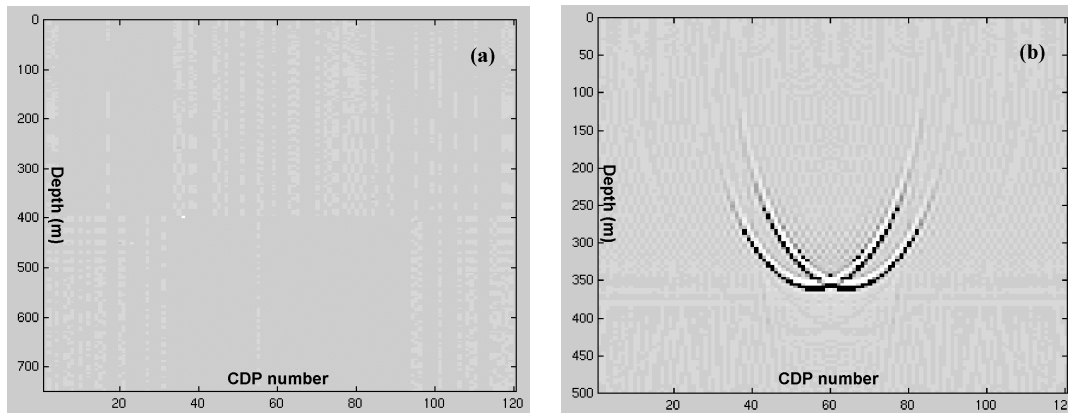


Figure 5: (a) The difference of two migration responses in figure 3 and (b) the superposition of the two migration responses shown in Figure 4. The average amplitude in the difference section (a) here is about 0.00013% of the average amplitudes in the responses in Figure 3.

Figure 5 shows two results to further clarify the similarity of the two responses in Figure 3 and the difference of the two responses in Figure 4.

A practical advantage of the migration for non-mode-conversion case is that, traces with negative and positive offsets can be binned only according to the absolute offset values before migration, which is not valid for the converted wave case.

### *Non-zero elements in migration filters*

As mentioned in previous sections, the non-zero zone in a migration filter moves when the migration velocities change. For same size of data sets for P-P wave and P-S wave from the same area, the migration velocities for converted wave case will be slower. This implies that the range of ray parameters where the migration filters have non-zero elements for P-S data will be larger than the one for P-P data. Whenever there are non-zero elements in migration filter, the filter must be computed, so that we have to compute more migration filters for P-S data case than for P-P data case.

### *Computation cost*

As discussed above about the computation of the migration filters, as a matrix function of two variables  $k_x$  and  $k_h$ , the migration filters have different symmetries for mode-conversion case and non-conversion case. Usually, 4 input traces have exactly the same migration filter for the non-mode-conversion case, while only 2 traces have the same filter for the converted wave case. The computation cost doubles when mode conversion is considered.

In addition, two phase-shift term tables have to be built for mode-conversion case, while for non-conversion case, only one table is needed. This make considerable memory size difference.

### **Zero time and zero offset: the imaging condition**

In the derivation of the migration formula in the previous section, i.e., from equation (13) to equation (14), we just simply set  $t=0$  and  $h=0$ . This is always correct mathematically. But in the computation of discrete Fourier transform, it is usually assumed that the first element in the forward transformed vector is the DC (zero frequency or wavenumber) term. And the first element in the inverse transformed vector is also the zero time or spatial location (such as depth or offset, or CDP in locations for our case).

If the start time on input traces is not zero, then the summation over the frequency of the discrete Fourier transformed traces will not provide the wavefield at zero time. Padding samples to make the input traces starting at zero time may be needed to ensure consistency between the imaging condition and the discrete Fourier transform algorithm.

The same problem occurs with the imaging condition on offset for the pre-stack case. Because the offset samples almost never start at zero in normal seismic data, it may be necessary to either phase-shift in offset direction or pad traces for the imaging condition. Instead of computing every time for different starting offsets or padding too many traces, three options are used to handle this offset shifting problem, which are (1) there are only positive offsets, (2) there are only negative offsets and (3) there are both positive and negative offsets.

### **Zero padding: three directions**

The  $V(z)$  f-k algorithm for pre-stack migration in CDP coordinates requires Fourier transformation in three dimensions: time, horizontal space (CDP) and source-receiver offset. The fast Fourier transform (FFT) requires equal spacing sampling, it may be necessary to insert some traces (usually zero traces). Most of the time this happens only in the offset dimension. Also, Fourier transform theory is based on the periodic functions which requires extending the size of the data in all the dimensions to avoid wrap-around effects.

Usually, performing a 3-D Fourier transform for a volume of data is faster than performing 1-D Fourier transforms consecutively on three dimensions. This is not true for our algorithm for pre-stack migration in CDP-offset coordinates. Very often zero padding doubles the size of the data so a 3D Fourier transform may spend more than half the time to do the transform on zero traces. Performing 1-D Fourier transform on each input trace (properly padded) before padding traces in offset direction, and then performing 1-D transform in offset before padding traces in CDP direction will not do any Fourier transforms on zero-element vectors in any of the three directions. This actually saves computation time.

## **APPLICATIONS AND DISCUSSIONS**

The application of pre-stack  $V(z)$  f-k method to many synthetic data examples shows that the algorithm has very high accuracy. Some results from Blackfoot-III vertical and radial data are also shown.

### **Synthetic data examples**

#### *The “broken hockey stick”*

This set of synthetic data is modeled from a constant velocity subsurface with one dipping reflector connected with a segment of flat reflector, like a hockey stick, and a point reflector (the puck?). The dipping reflector has a dip about 45 degree and has a gap (broken?) in the middle. The modeling velocity is 10,000 feet per second.

Figure 6 shows the stacked section with a wide range of stacking velocities (from 10,000 ft/s up to 57,000 ft/s) along the line. The point reflector can be recognized by the diffraction hyperbola. The dipping reflector and the short flat segment are both properly stacked. The gap in the dipping reflector is smeared, although it can be noticed that there may be some “anomalies” along the dipping reflector. Migrating this section by both Stolt’s f-k method and Kirchhoff method with the wave propagation (modeling) velocity showed that post-stack migration may not be capable to resolve the gap. The migration results are not shown here. It is possible that DMO may help post-stack migration to provide better results.

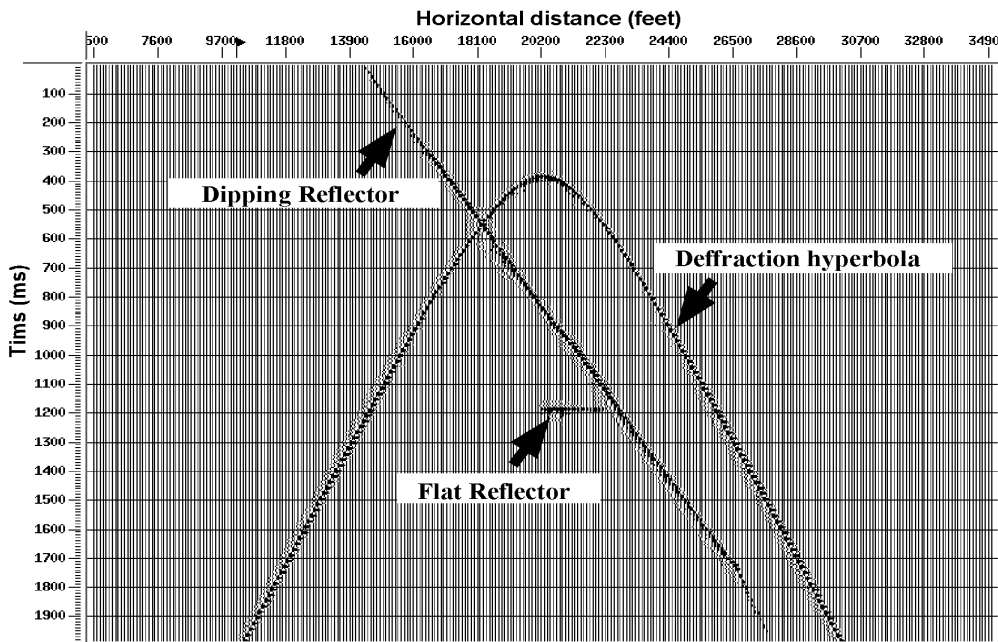


Figure 6: The stacked section of the “broken hockey stick” data. The stacking velocity was picked for every 20 CDP locations (2000 feet apart). The stacking velocity ranges from the accurate wave propagation velocity (10,000 ft/s) up to 57,000 ft/s. It can be seen that, the scattered diffraction, the flat and dipping reflectors are all well stacked. But the gap in the dipping reflector is smeared, although it is recognizable that there may be some “anomalies” along the reflector.

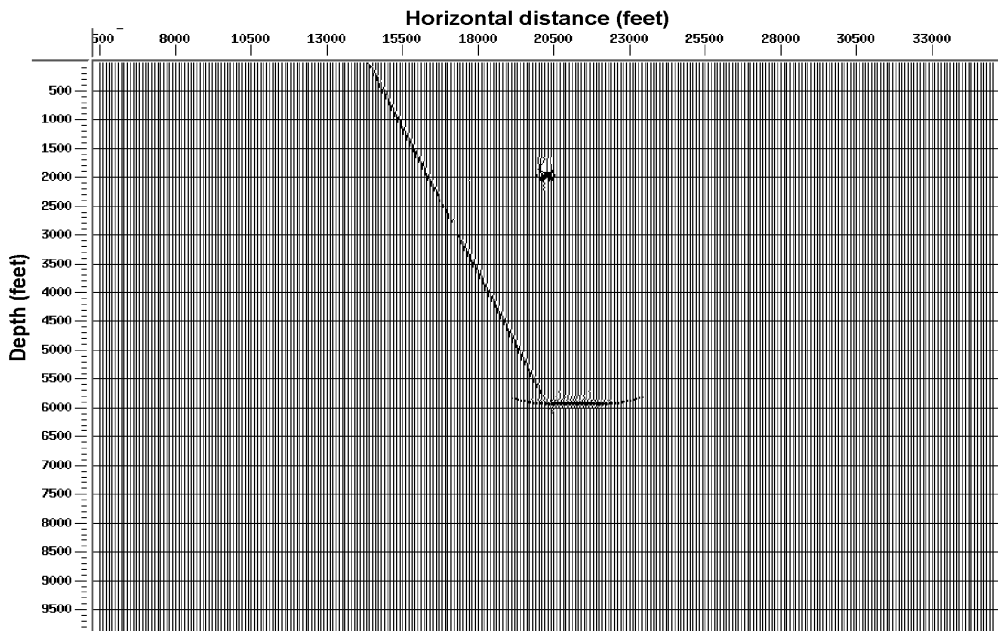


Figure 7:  $V(z)$  f-k pre-stack migration of the “broken hockey stick” prestack synthetic data. The migration velocity is 10,000 feet per second, which is the accurate velocity used for modeling the data set. With the stacked section shown in Figure 6 as a comparison, this image result is very good. Not only the dipping reflector is properly located, and the scatter point is highly focused, the gap in the dipping reflector is also clearly resolved.

Figure 7 shows the result of  $V(z)$  f-k pre-stack migration using the accurate velocity, 10,000 feet per second. Apart from some migration artifacts at the ends of the flat reflector, the imaging is very good. Not only the dipping reflector is properly located, and the scatter point is highly focused, the gap in the dipping reflector is clearly resolved.

*One curved reflector*

The earth subsurface model shown in Figure 8 contains only one curved reflector. The maximum dip along the reflector is more than 45 degrees. The layers above and below the reflector are assumed isotropic. The P wave and S wave velocities in the upper layer are 1800m/s and 900m/s respectively, and the P wave and S wave velocities in the lower layer are 3000m/s and 1200m/s respectively.

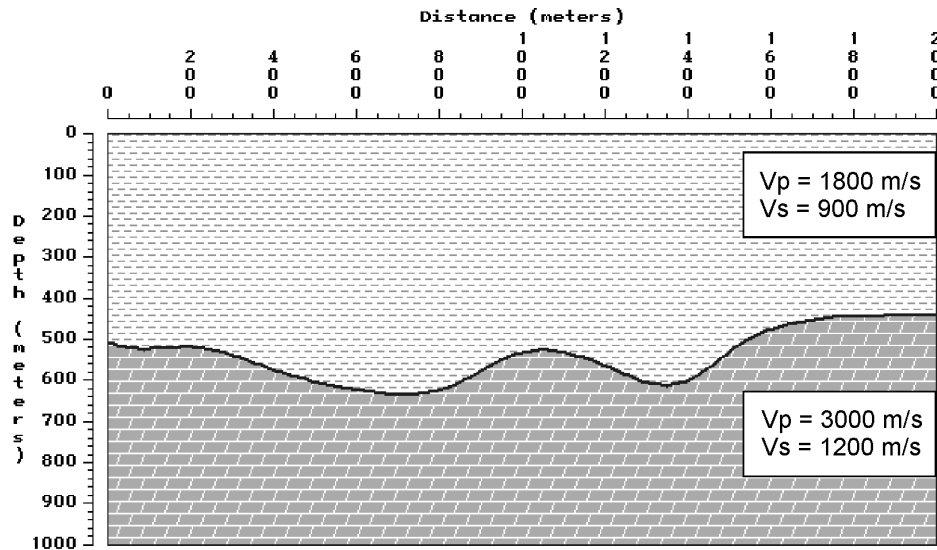


Figure 8: An earth subsurface model with one curved reflector. The two layers above and below the reflector are assumed isotropic.

The geometry of the source and receiver spreads has 41 shots at a 25 meter interval from 500 meters to 1500 meters, and 161 receiver locations from 0 to 2000 meters with an interval of 12.5 meters. At each receiver location, there are two channels connected to a vertical geophone and a radial geophone. All the geophones at all the receiver stations are activated for all the shots. Thus, the CDP range is from 250 to 1750 meters, and the fold is high. From this model, two sets of synthetic data are obtained, one is P-P data from the vertical channel and the other is P-S mode-converted data from the radial channel.

Figure 9 and Figure 10 show the results of  $V(z)$  f-k migration results of the P-P data and the P-S data respectively. There are some artifacts in both results, but the basic images are clear.

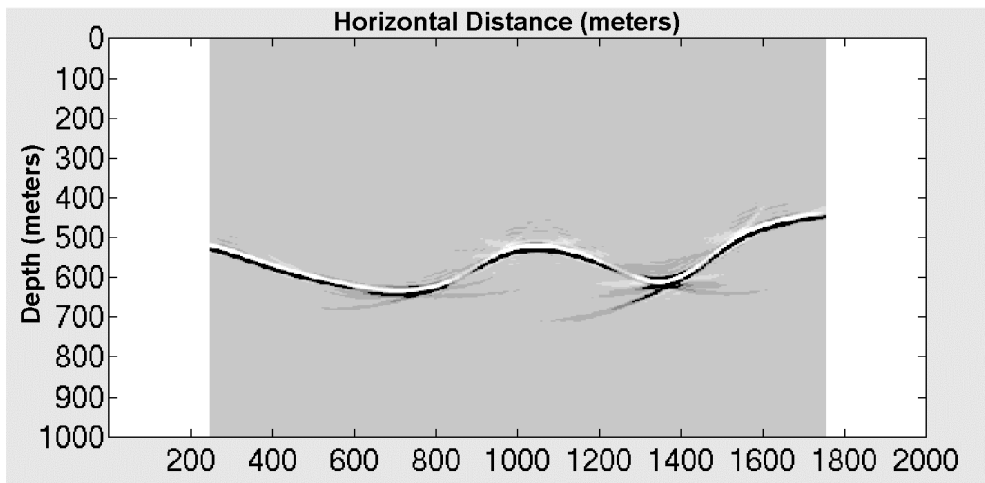


Figure 9:  $V(z)$  f-k prestack migration of the P-P data acquired from the model in Figure 8.

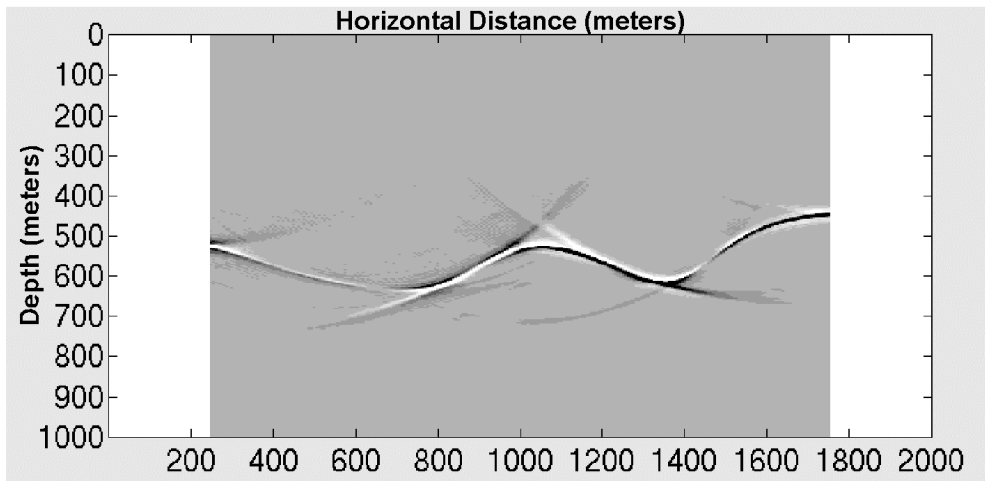


Figure 10:  $V(z)$  f-k prestack migration of the P-S data acquired from the model in Figure 8.

### Experiments with Blackfoot-III 20 meter data

The Blackfoot-III 20meter data has three receiver components. The migration experiments with  $V(z)$  f-k method used vertical (P-P) data and radial (P-S) data. Both vertical and radial data have been processed by Matrix Geophysical. The datasets used for migration experiments are those ready for final stack, which are already properly amplitude gain recovered and deconvolved, and the statics are estimated and applied. The experiments show the migration results using different velocity functions. The target is the imaging of the Glauconitic sand channel at a depth about 1520 meters.

#### *P-P data: velocities from RMS stacking velocity or from well log*

The current  $V(z)$  f-k implementation requires the input velocity function be given as interval velocity in depth. The interval velocity can be computed from the stacking velocity using Dix's equation, or directly from well information.

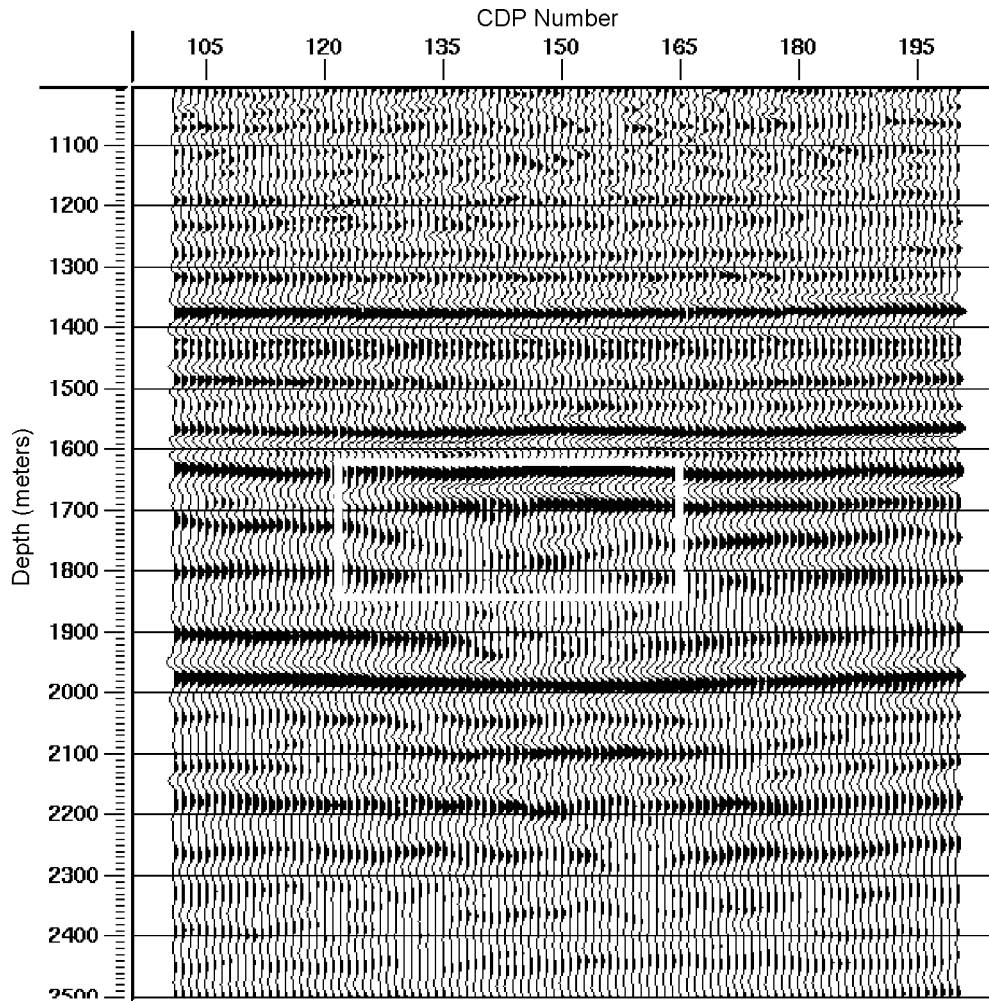


Figure 11: The  $V(z)$  f-k prestack migration result of the Blackfoot-III 20-meter vertical data. The migration velocity is obtained by converting the stacking velocity (from Matrix Geophysical) into depth interval velocity. The target channel area is boxed.

Figure 11 shows the  $V(z)$  f-k migration result with the depth interval velocity computed from the final stacking velocity observed by Matrix Geophysical. The horizontal location of the channel is about 120 to 160 in CDP numbers, and for emphasize, the channel area is boxed in the Figure. Although the image of the channel is very clear and easy to identify, it is noticed that the migration result gives a channel image at about 200 meters too deep. This suggests that the migration velocity used might be too high.

Figure 12 shows the result of  $V(z)$  f-k migration by using the velocity information from the well log in the area. The well log gives only the information from depth 220 to 1600 meters. It was assumed that the wave velocity at the depth shallower than 220 meters is isotropic and with a constant velocity value such that the target channel will be at the right depth. The velocity after 1600 meters is the same as used for the result in Figure 11.

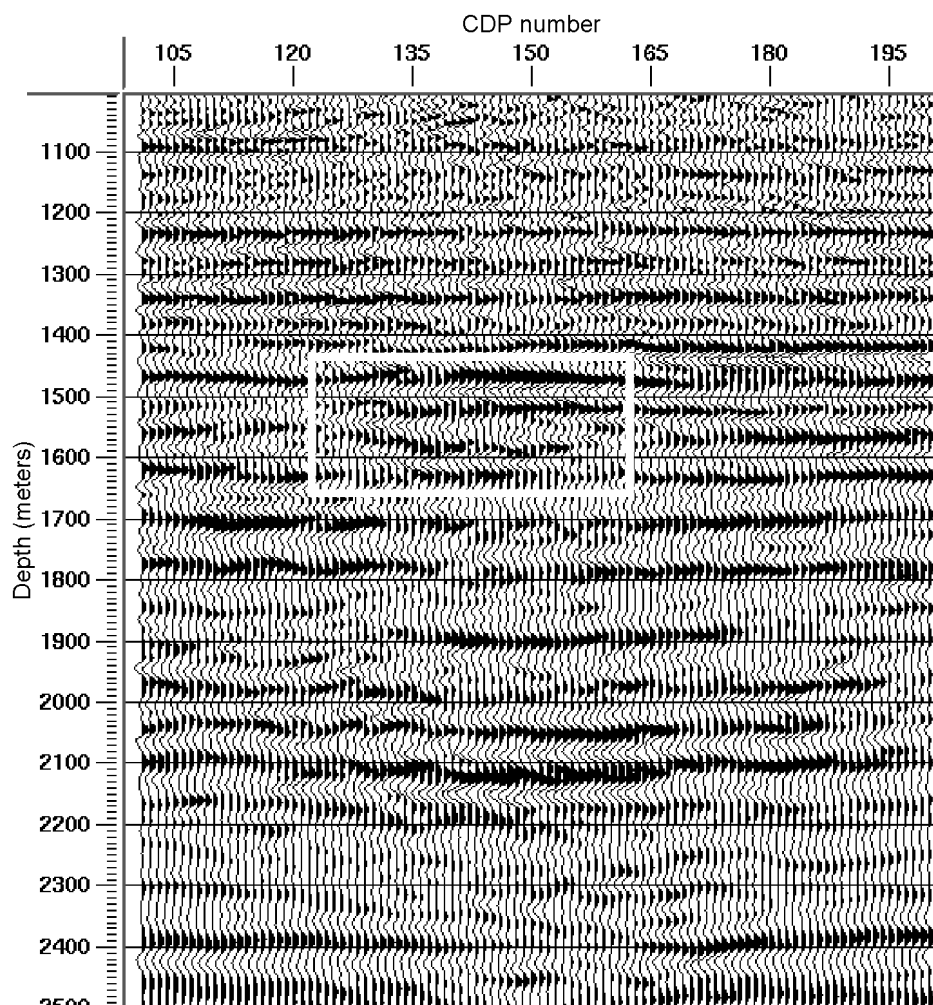


Figure 12: The  $V(z)$  f-k prestack migration result of the Blackfoot-III 20-meter vertical data. The migration velocity is obtained using the well log information. The near surface velocity is assumed constant, while the velocity at layers deeper than the well keeps the same as that used for migration shown in Figure 11. The target channel area is also boxed.

In Figure 12, the imaged depth of the target is correct, but comparing to the imaging shown in Figure 11, not only the channel was not imaged clearly, the entire section is also much noisier. The events other than the channel area were not properly imaged either. At first, it was expected that the depth difference of the target channel might be caused from the differences between the well velocity and the converted stacking velocity. However, this is not the case.

For further discussion, the migration velocities used to obtain the migration results shown in Figure 11 and Figure 12 are analyzed in more detail. Figure 13 shows the two interval velocities (as functions of depth). The difference between these two velocities is not significant except in the first 220 meters. The converted stacking (RMS) velocity is more like a smoother version of the well velocity. The converted stacking velocity, which results in the deeper target image, is not faster at all. In fact, in the depth range with well information available (220 to 1600 meters), the traveltimes calculated from the well velocity is even longer.

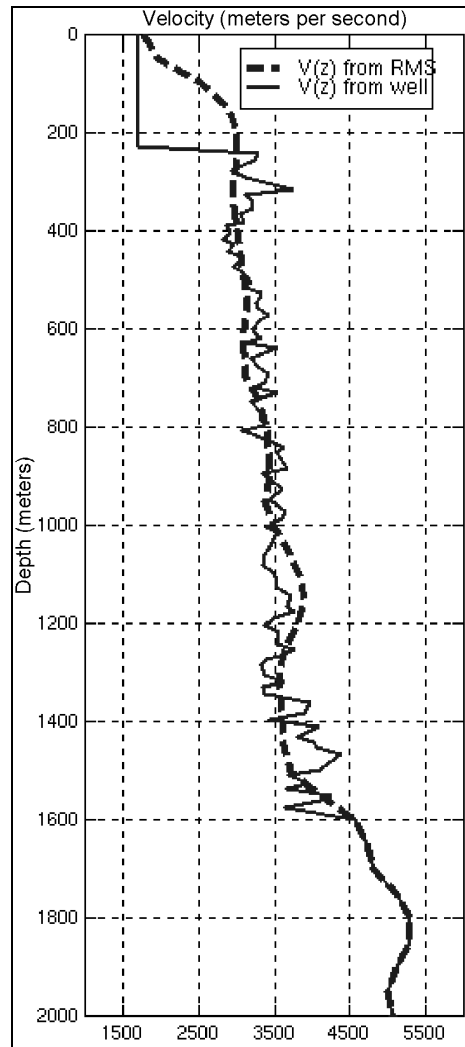


Figure 13: Migration velocity functions used for the results shown in Figure 11 and Figure 12. The wider dashed curve is the velocity converted from the stacking velocity, the thinner solid line is the detailed blocked well velocity plus some extra values before 220 meter depth and after 1600 meter depth. The two velocity functions are exactly the same after 1600 meter, so the values after 2000 meters are not shown.

For efficiency, the prestack P-P data is further processed for later migration results. Besides trace equalization, which was also applied for results in Figure 11 and Figure 12, a weak f-x prediction filter is applied on shot gathers prior to migration. Then, a bandpass filter with 4 corner frequencies 5, 8, 80 and 100hz and an AGC with window length 500 ms are applied. In addition, the data is desampled into 2 ms rate, while the original sample rate is 1 millisecond. The computation cost was greatly reduced, and the later results show that the imaging quality is well preserved.

The next  $V(z)$  f-k migration experiment is done with a velocity function combined from the two velocities in Figure 13. The new velocity function equal to the one converted from stacking velocity at the depth shallower than 220 meters and depth deeper than 1600 meters, while at the depth between 220 and 1600 meters (where the well information is available), the blocked well velocity is used. Figure 14 shows the imaging result.

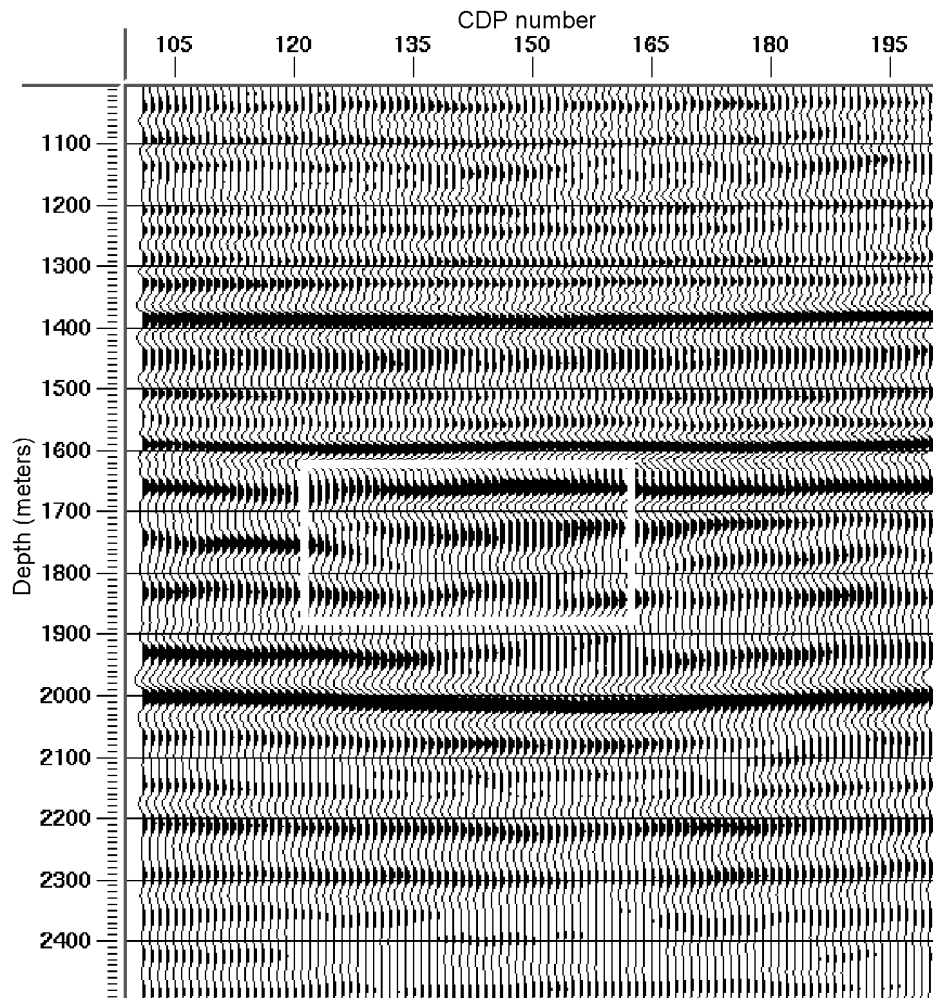


Figure 14: The  $V(z)$  f-k prestack migration of the P-P data with the combined velocity from the two velocities used for the images shown in Figure 11 and Figure 12. The blocked well velocity is inserted into the converted stacking velocity between 220 and 1600 meters. Also, the data for migration is weakly filtered and the bandwidth is limited to 5-8-80-100Hz. The channel area is boxed.

In Figure 14, the data is cleaner than both the one in Figure 11 and Figure 12. The image of the channel area is not as good as the one migrated with converted stacking velocity (Figure 11), but better than the one using the velocity which matches the depth of the Glauconitic channel (Figure 12). It is also noticed that the channel in Figure 14 and the channel in Figure 11 have only about 20 meters difference in depth. This implies that the 200 meters difference between the channel depth in Figure 11 and Figure 12 is mainly because of the differences of the migration velocities at the first 220 meters.

The imaging of the channel in Figure 14 is not as good as the one in Figure 11. This is not because of the filtering effects on the data before migration, but the differences between the well velocity and the converted stacking velocity. This is further proved by the imaging result shown in Figure 15, which use the converted stacking velocity again, but on the filtered data.

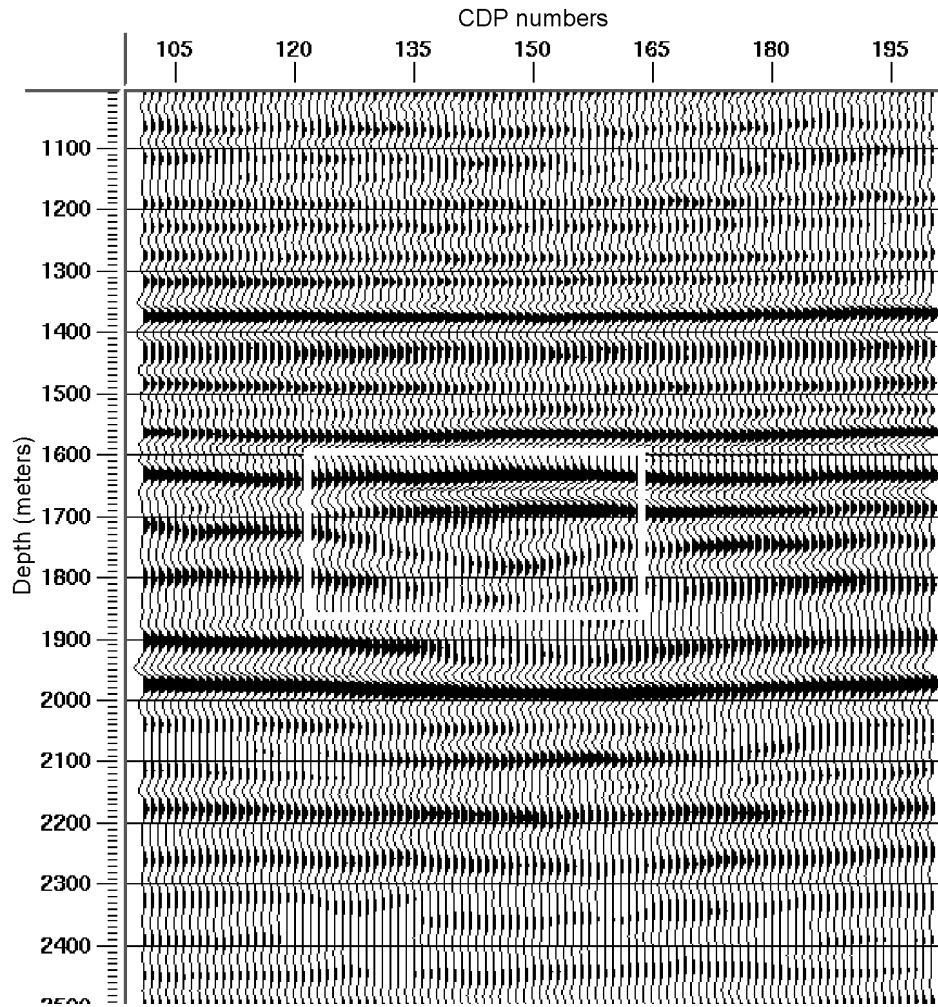


Figure 15: The  $V(z)$  f-k prestack migration of the filtered data using the converted stacking velocity, which is the same as the one used for Figure 11. The imaging is even more focused than figure 11. This at least implies that the filter applied on the data before migration did not reduce the imaging capability of the data.

As a summary, there is still a question about these experiment results. Why is the best imaging velocity not the velocity which puts the target at the right place? Comparing the two velocity functions shown in Figure 13 and the two images in Figure 11 and Figure 14, it is clear that the incorrect depths of migration images are not because of the difference between well velocity and converted stacking velocity. They result from the difference of the migration velocities at the depth shallower than well logging depth (220 meters). This implies that the answer of the question maybe lies in the datuming problem. That converted stacking velocity gives very a good image may be because stacking velocity is not sensitive to the small errors in datuming.

When the best imaging velocity is available, and the depth of the target is known, it is easy to get a reliable time and depth image with conversions between time and depth after migration. Figure 16 is a time domain version of the image shown in Figure 15.

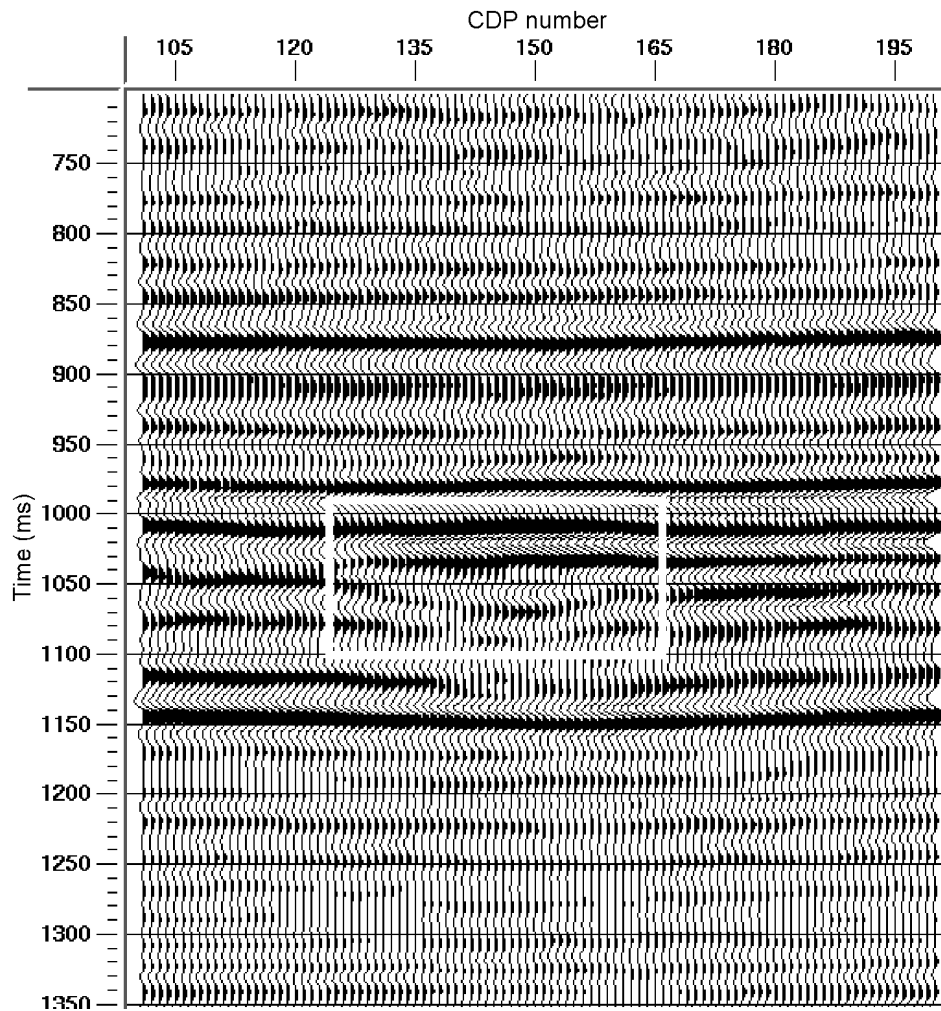


Figure 16: The depth to time conversion of the image in Figure 15. The conversion velocity is the migration velocity which gives the best imaging. The channel area is again boxed for comparison.

*P-P data: post stack migration or prestack migration*

For seismic data from plain areas like Blackfoot, Alberta, regular processing often does not include prestack migration. Many examples show that, prestack migration does gives better imaging when it is used.

Figure 17 shows the stacked section with the final stacking velocity observed by Matrix Geophysical, the input for the stacking is the 2 ms sample filtered data. Figure 18 shows the results of post-stack phase-shift migration with the converted stacking velocity. The channel areas in both sections are boxed for comparison.

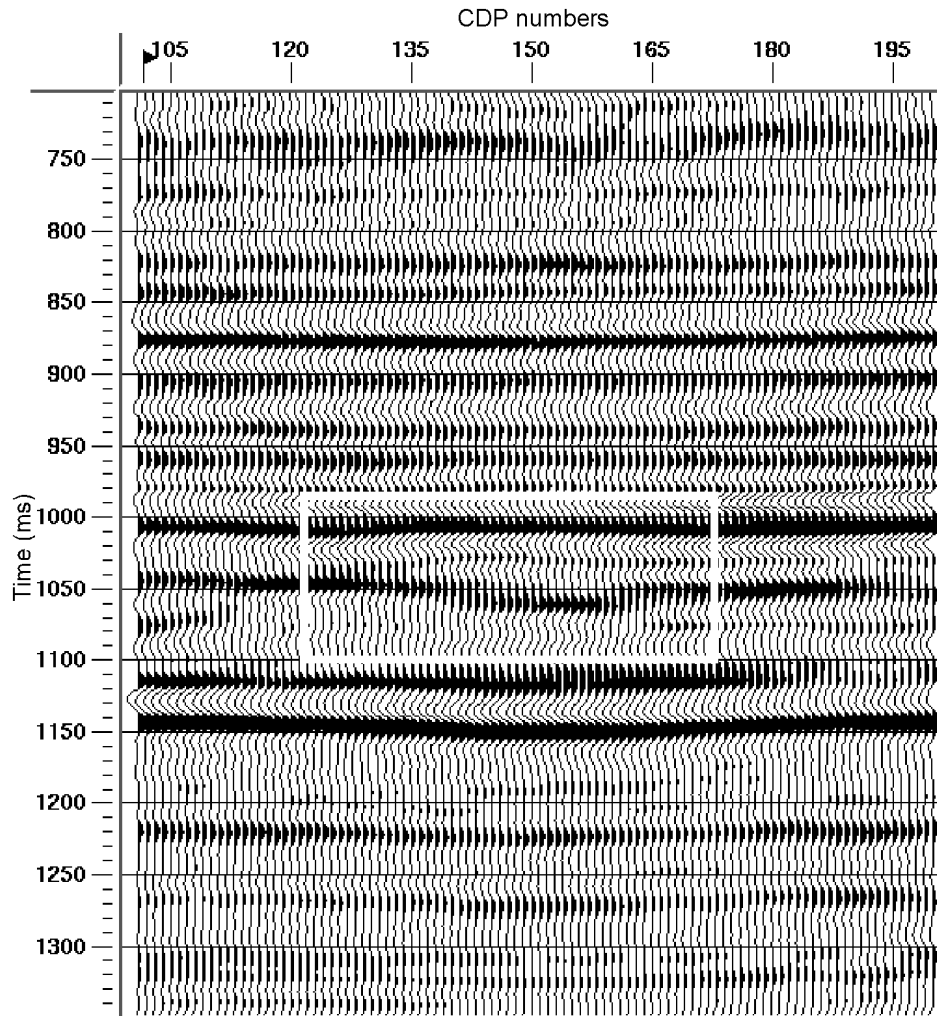


Figure 17: Stacked section of the filtered P-P data with the final stacking velocity observed by Matrix Geophysical. The channel area is boxed for comparison.

It can be seen that although the stacked section had very good quality, the events in the target channel area are very clear although they are not well shaped. The post-stack migration (Figure 18) can not resolve the channel shape very clearly, as the prestack migration does (Figure 16).

Mathematically, the current implemented version of  $V(z)$  f-k migration is the same as the phase-shift migration, including the assumption and formulation, the comparison between our  $V(z)$  f-k prestack migration (Figure 16) and the post-stack phase-shift migration is reasonable.

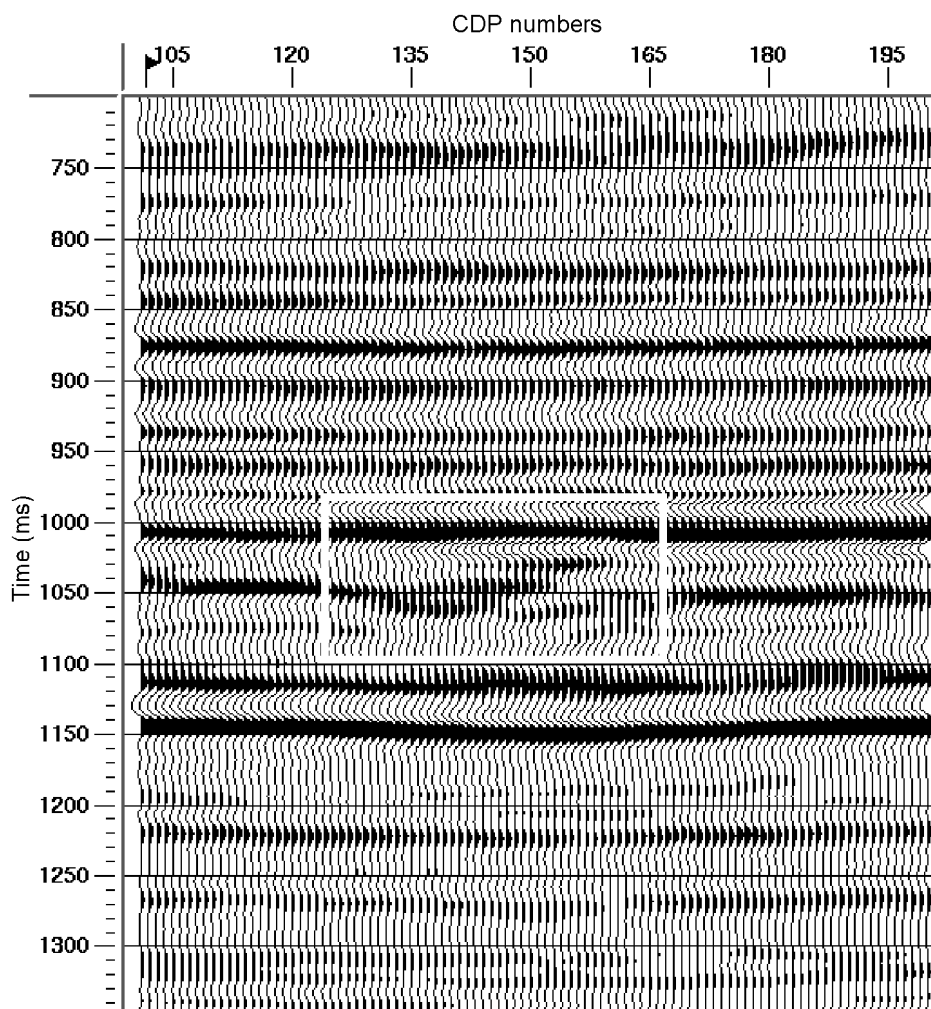


Figure 18: Post-stack phase-shift migration of the stacked section shown in Figure 17. Comparing to The prestack  $V(z)$  f-k imaging shown in Figure 16, this result does not resolve the channel area (boxed) very clearly.

#### *P-S Data: offset orientation and velocity*

One of the difficulties to migrate a set of converted-wave data is the effects of offset orientation. When the wave velocity changes only in depth, for P-P data, besides the imaging quality, the migration may only position the events at the wrong depth due to the velocity error. While for the converted wave data, velocity errors not only result in a bad image and the wrong depth, but also the wrong lateral locations. Even worse, due to velocity error, the lateral position of the same target moves in opposite directions for positive and negative offset traces. In these cases, the summation of the images from positive and negative offset data may degrade the imaging quality, instead of enhancing the final image.

Figure 19 (on page 29) and Figure 20 (on page 30) show the results of  $V(z)$  f-k migration from the negative offset data and the positive offset data respectively. As expected, the energy is moved away from the CMP location to the direction where the receivers are located, and the magnitude of this energy displacement changes with the depth.

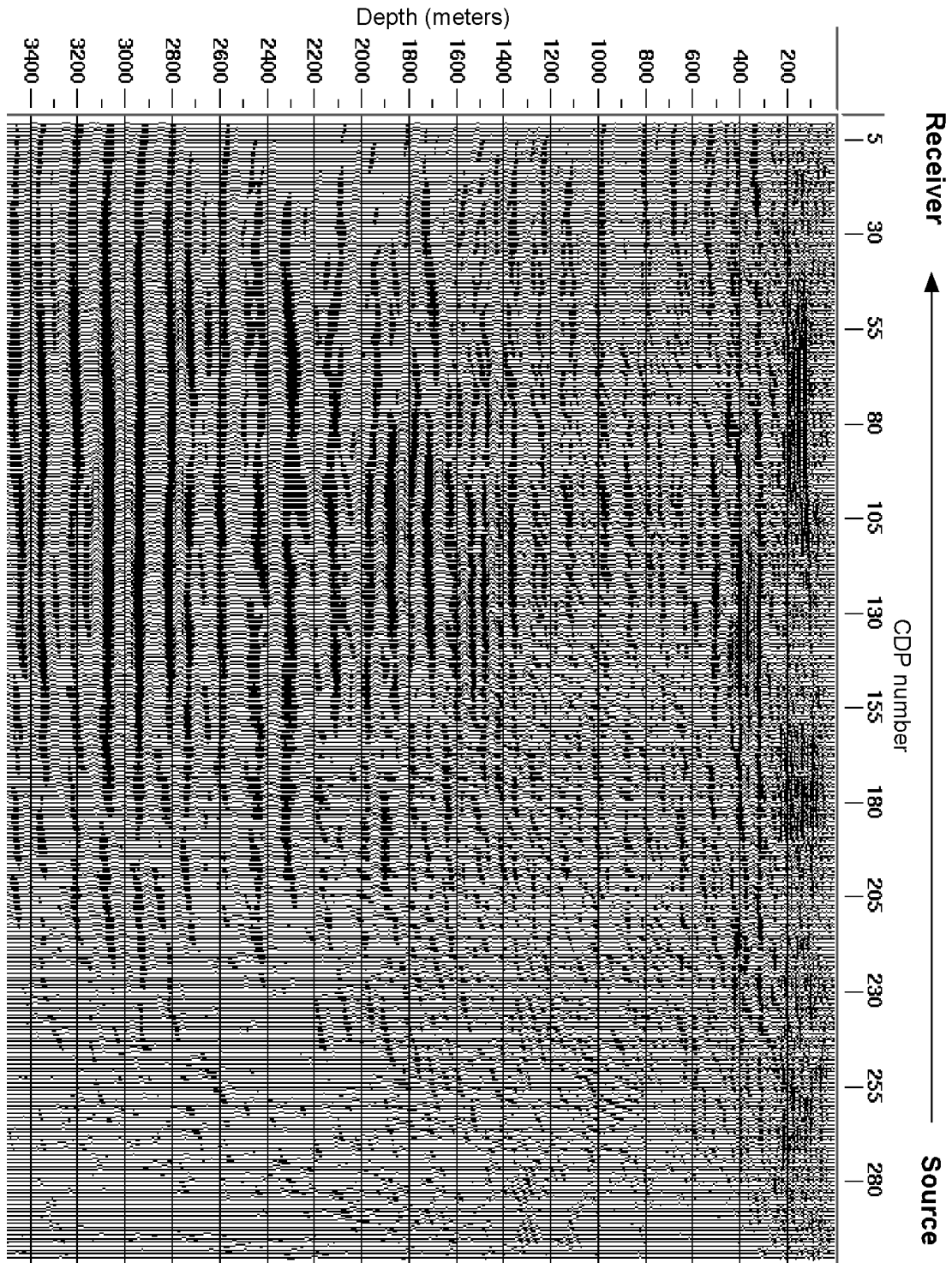


Figure 19: V(z) f-k migration from the traces in the radial data with negative offsets only. This data is shown here without AGC or trace equalization in order to tell how the migration fold is distributed. The energy at one CMP location is tends to be moved to the direction where the receivers are.

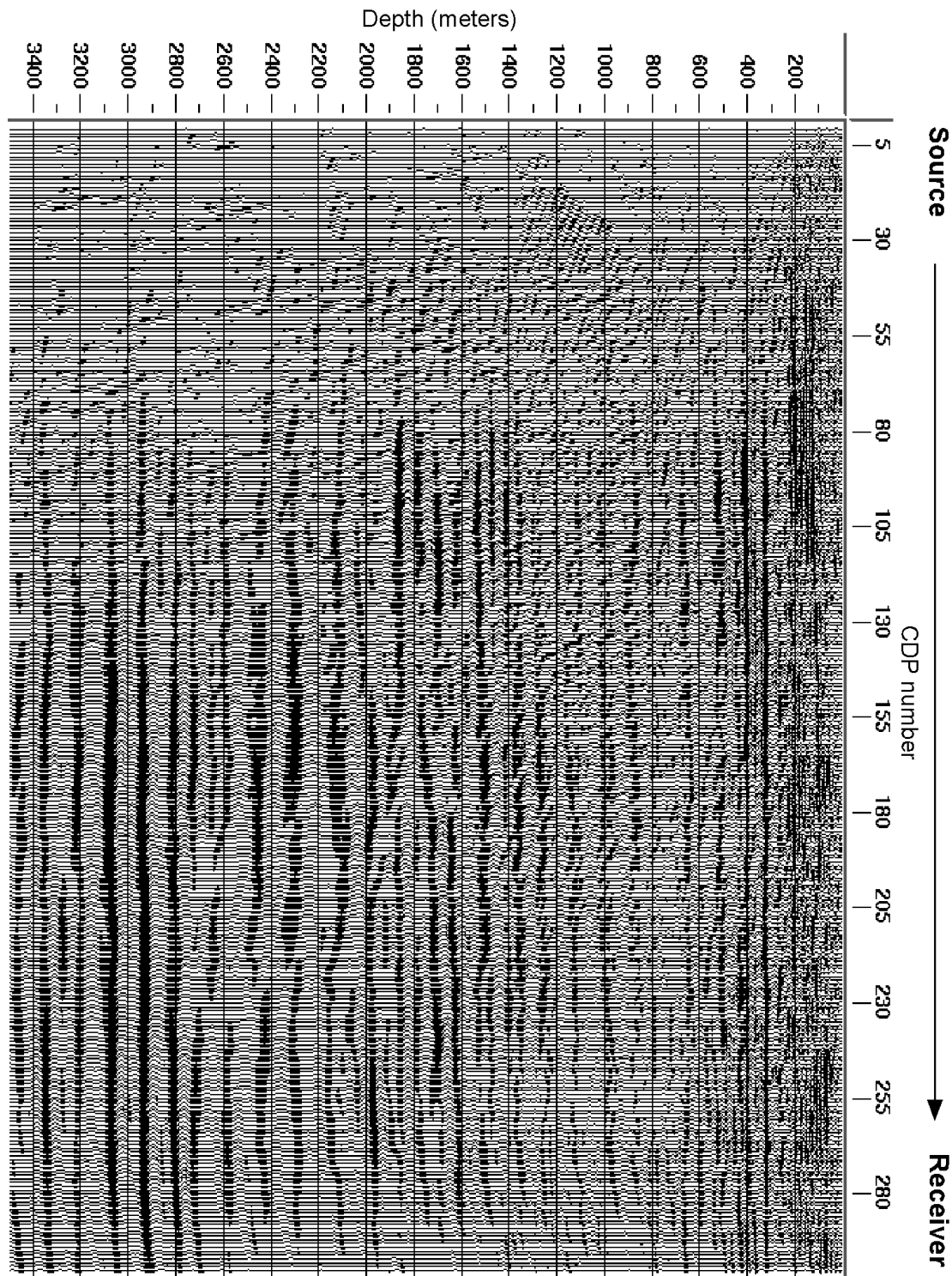


Figure 20:  $V(z)$  f-k migration from the traces in the radial data with positive offsets only. This data is shown here without AGC or trace equalization in order to tell how the migration fold is distributed.

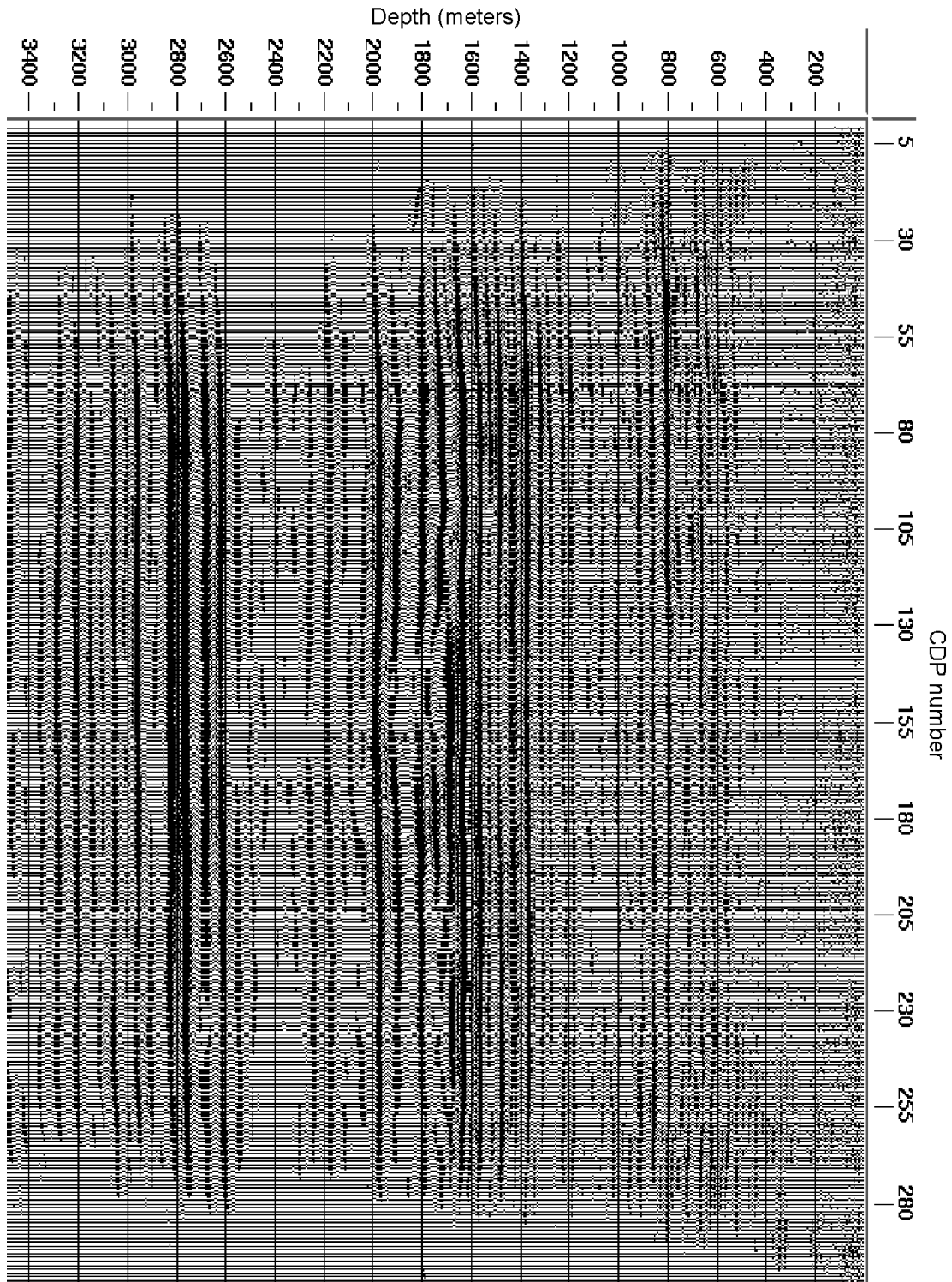


Figure 21: V(z) f-k migration from vertical data. Figure 16 is just the middle part of this migrated section. As a comparison with the sections shown in Figure 19 and Figure 20, this section is shown without AGC or trace equalization in order to tell how the migration fold for P-P is distributed.

The overall amplitudes in figures 19, 20 and 21 are proportional to the final migration fold because the input data was trace-equalized. Comparing the migration fold distributions in Figure 19 and Figure 20, it is evident that the energy of a seismic trace in converted wave data at some CMP location tends to be moved to the direction where its receiver is. The migration fold changes not only in depth direction, but also changes laterally, which is different for positive and negative offsets. As a comparison, in the migration result from P-P data, which is shown in Figure 21, the changing of migration fold is mainly vertically. It is clearer to see at the deeper depth, where the PP migration fold keeps in a smaller (comparing to the shallower depth) range in the middle of the line, where the CDP fold is higher. In both positive and negative offset migration for converted-wave data, the folds keeps high until one edge of the line, although each offset is at a different edge.

For the analysis of the imaging quality of target channel from converted wave data, the target area in both Figure 19 and Figure 20 are zoomed and shown in the following Figure 22 and Figure 23 respectively.

In Figure 22, which shows the channel area of the  $V(z)$  f-k migration from the negative offset traces, a solid line is drawn to follow the possible channel bottom. As a comparison, a dashed line is also shown which is the solid line in Figure 23, which is the migration from positive offset traces. The differences between the two lines are small not explained yet.

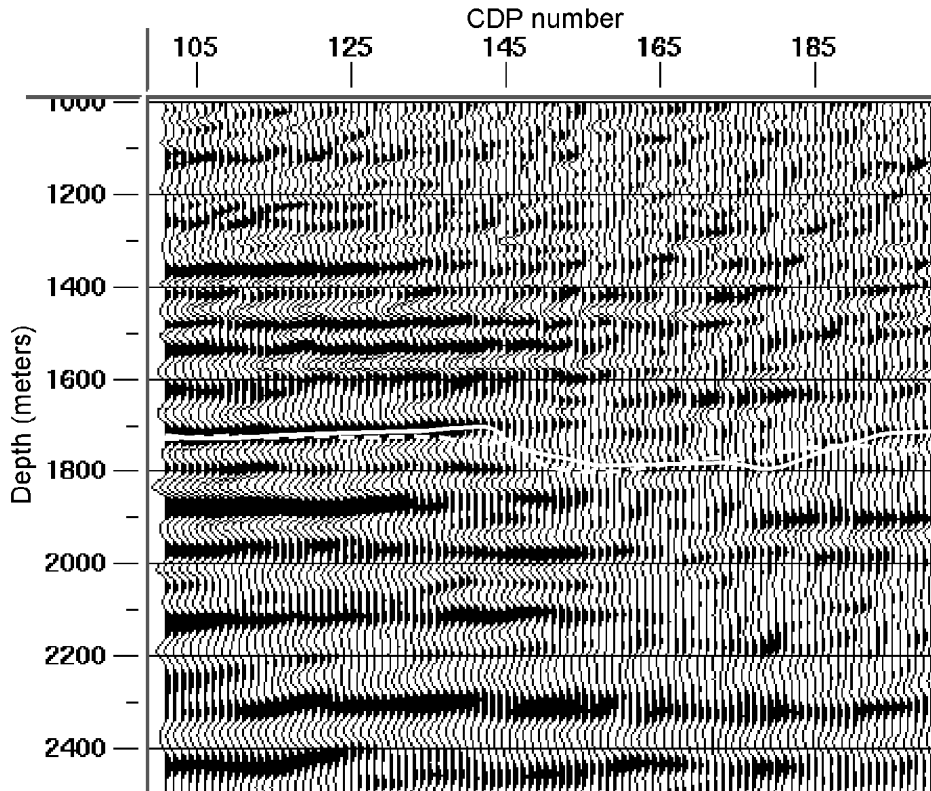


Figure 22: A part of the Figure 19. The possible channel bottom is followed by a solid line. While the dashed line is a copy of the solid line in Figure 23, in which the channel bottom is interpreted differently.

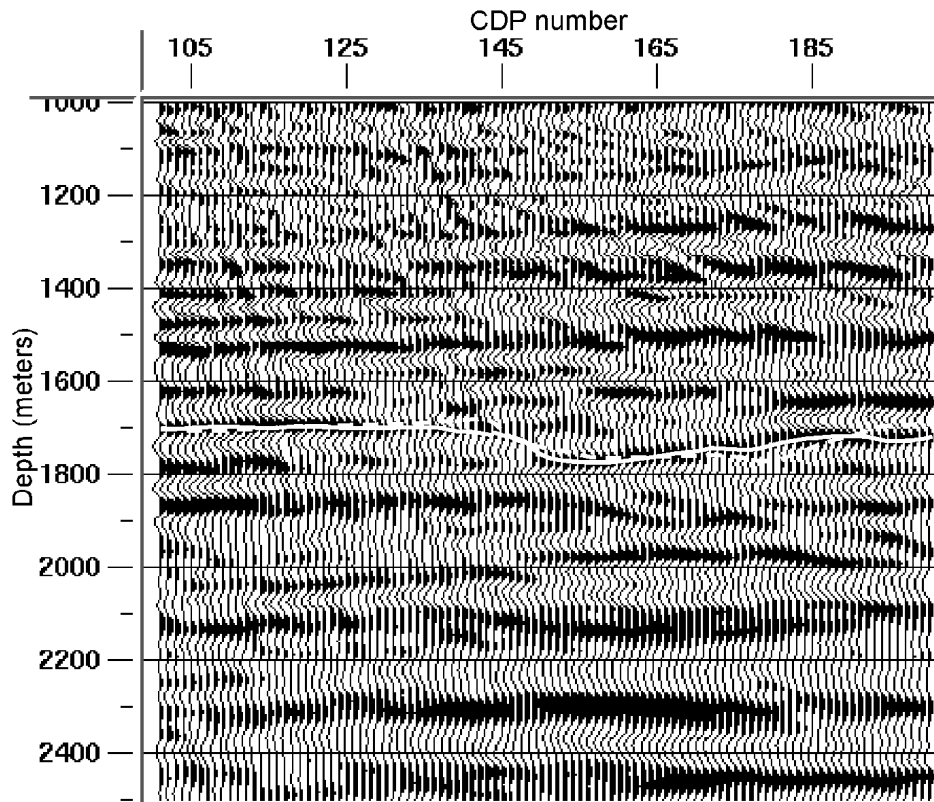


Figure 23: A part of the Figure 20. The possible channel bottom is followed by a solid line. The dashed line is a copy of the solid line in Figure 22, in which the channel bottom is interpreted differently.

As a summary, the  $V(z)$  f-k migration of the whole converted wave prestack data is shown in Figure 24. It is mathematically the direct summation from the two migrated sections shown in Figure 22 and Figure 23. The two interpretations of the channel bottom are shown in very thin lines so that the characters of the events can also be seen.

As noticed, the depths of the channel are about 200 meters deeper than its geological depth, and the interpretations may be wrong. These experiments highlight some aspects of concern for the prestack migration of converted-wave data.

### CONCLUSIONS AND FUTURE WORK

The  $V(z)$  f-k migration for prestack PP and PS data is implemented as a module in ProMAX. Many synthetic data and real data experiment shows that this module works, and it provides high quality migration results.

The algorithm is currently implemented in the Fourier domain so that the theoretical advantages of the algorithm can be investigated. Although the current algorithm mathematically has no difference from the conventional phase-shift migration, the introduction of the nonstationary filter concept may help extending the method further to both more efficient and theoretically more accurate directions.

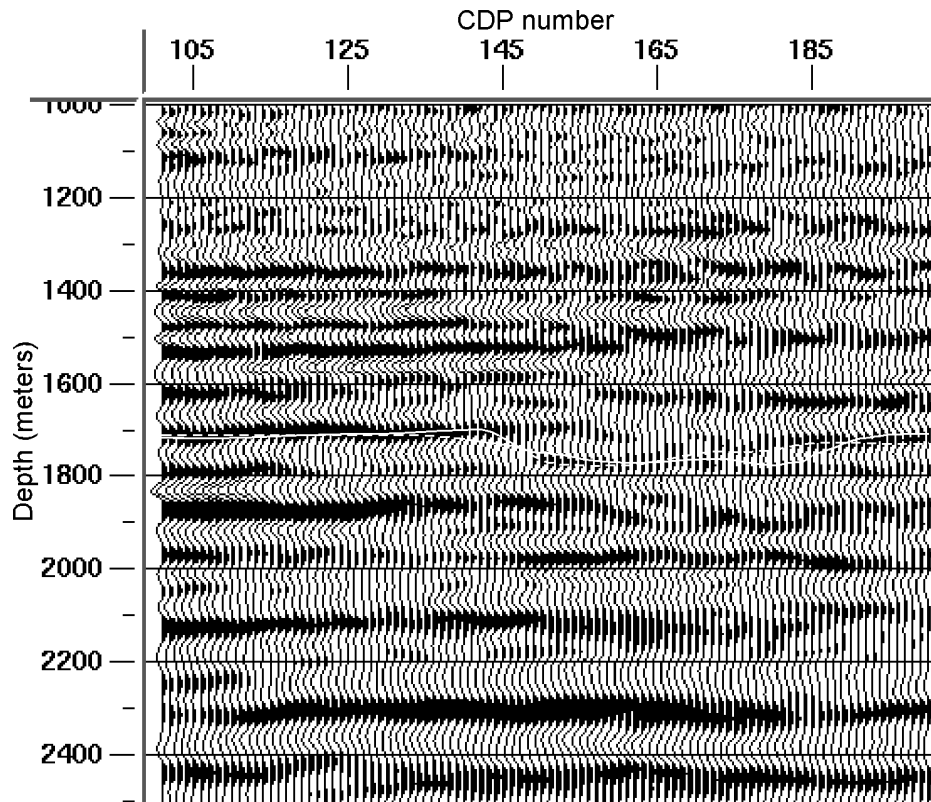


Figure 24: The  $V(z)$   $f$ - $k$  migration of the whole converted wave prestack data. It is not the direct summation from the two migrated sections shown in Figure 22 and Figure 23, but theoretically it should be. The two interpretations of the channel bottom are shown in very thin lines for not overriding the characters of the events.

As mentioned in this report, this algorithm can be implemented as a mixed-domain non-stationary filter, which should be more efficient.

The current implementation only considered the ray angle up to 90 degrees, and the evanescent energy is simply ignored. As a Fourier domain migration, it is easy to include the evanescent energy and ray angles beyond 90 degrees in the migration process.

This  $V(z)$   $f$ - $k$  method can be implemented as an algorithm applied on shot gathers. It will be more efficient at least in handling the Fourier transform and computer memory.

There are some possible ways to compute the migration filters in some approximate manner. This should save a significant amount of computation cost, because the most of the computation in the current algorithm is to prepare the filters.

The further theoretical extension of this method might be the accommodation of the lateral velocity variation. This could lead to a very accurate prestack depth migration.

Combined with the correlation analysis of P-P data and P-S on migration depth section, this method, on the other hand, can be used as a tool to get more accurate S wave velocity or more reliable P to S velocity ratio.

Migration to multi-offset sections is also a direction to extend this method. Accurately migrated offset sections may provide more accurate AVO information.

### **ACKNOWLEDGMENT**

We thank the sponsors of the CREWES Project for their financial support. Mr. Henry Bland and Mr. Darren Foltinek are very much appreciated for their help in programming and system support. The data information from Mr. Brian Hoffe and Dr. Larry Lines has been very helpful.

### **REFERENCES**

- Claerbout, J.F., 1985, *Imaging the Earth's Interior*: Blackwell Scientific Publications. Available over the internet at <http://sepwww.stanford.edu/sep/prof/>.
- Gazdag, J., 1978, Wave equation migration with the phase-shift method: *Geophysics*, 43, 1342-1352.
- Margrave, G.F., 1998a, Theory of nonstationary linear filtering in the Fourier domain with application to time-variant filtering: *Geophysics*, 63, 244-259
- Margrave, G.F., 1998b, Direct Fourier migration for vertical velocity variations, Extended Abstracts, SEG meeting, New Orleans, USA.
- Margrave, G.F., 1998c, Direct Fourier migration for vertical velocity variations, CREWES Research Report, Vol. 10.
- Stolt, R.H., 1978, Migration by Fourier Transform, *Geophysics*: 43, 23-48
- Yilmaz, O., 1987, *Seismic Data Processing*: Society of Exploration Geophysicists.